



University of
Stavanger

FACULTY OF SCIENCE AND TECHNOLOGY

MASTER'S THESIS

| | |
|---|---|
| Study Programme/Specialisation: Mathematics and Physics/Physics | Spring semester, 2020 Open |
| Author: Rashmi Dahal | |
| Programme coordinator: Eli Drange Vee Supervisor: Olena Zavorotynska | |
| Title of master's thesis: X-ray Studies on partially decomposed γ- Mg(BH₄)₂ | |
| Credits (ECTS): 60 | |
| Keywords: X-ray physics γ- Mg(BH₄)₂ X-ray absorption spectroscopy X-ray diffraction XAS XRD | Number of pages: 58 Stavanger, 15th June 2020 |

Preface

This is the final report of the research work of the master's thesis carried out through 2019 fall and 2020 spring semesters to complete the master's Program in Physics from the Department of Mathematics and Physics, University of Stavanger. The research subject is within Materials' science and is focused on the study of a hydrogen storage material with common X-ray techniques such as X-ray absorption spectroscopy (XAS) and powder X-ray diffraction (PXD).

Stavanger, Norway, 15th July 2020

Rashmi Dahal

Acknowledgments

The master's thesis has been submitted successfully on 15.07.2020. I would like to express my sincere gratitude to my supervisor, associate professor Dr. Olena Zavorotynska for her continuous encouragement and guidance with needed articles, books, useful hints and tips during the whole period of the thesis. I have been lucky to have a supervisor who always cared about my work and responded to my queries so promptly. I am deeply indebted to her as she is the one who opened the door of my experimental physics world through this thesis.

I would like to recognize the assistance that I received from our research lab engineer Ms. Anna Cecilie Åsland for the support to operate all the laboratory instruments and the corresponding software. I had a great time working with her.

A heartfelt thanks go to my husband, Mr. Milan Sanjel who always supported and nurtured me and always had a profound belief in my abilities.

A special thanks goes also to my family for making my idea of studying abroad possible. Especially my brother, Mr. Upendra Dahal who inspired me and supported all the times for this master's studies.

I greatly appreciate Dr. Stefano Deledda from the Institute for Energy Technology (Norway) for providing the gamma phase magnesium borohydride sample for the whole work.

Thanks go to all the professors from the Department of Mathematics and Physics, the physical and technical contribution of the University of Stavanger for providing the educational platform for my whole master's studies. The financial support for traveling to the synchrotrons is greatly appreciated.

XAS data for this experiment was collected on RGBL beamline at the BESSY II electron storage ring operated by the Helmholtz-Zentrum Berlin. I would particularly like to acknowledge the help and support of research scientists Anna Makarova and Dmitry Smirnov during the experiment and the financial support provided by the Synchrotron.

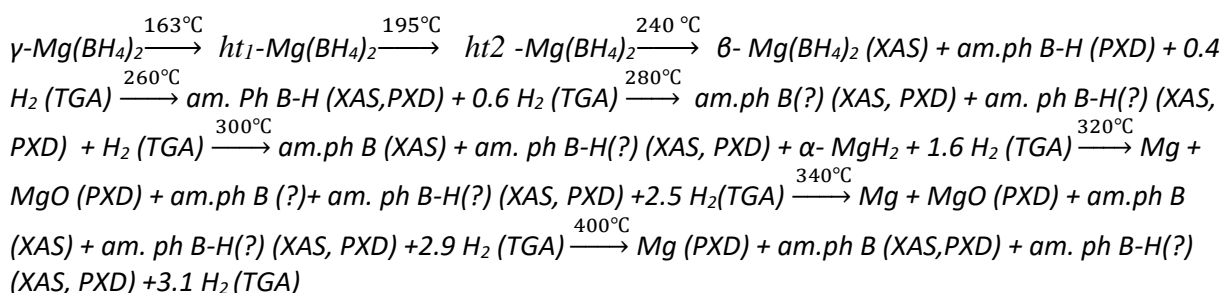
I must thank Synchrotron Elettra, Trieste, Italy for the funding that was provided even though the experimental part could not be carried out due to the technical problems in the Synchrotron.

Rashmi Dahal, 15th July, 2020

Summary

Hydrogen is the energy that fuels the sun and the stars. Having the potential to be zero-carbon during production, when produced by renewable resources, it is an attractive carrier of the pollution-free renewable energy. In this context, magnesium borohydride ($\text{Mg}(\text{BH}_4)_2$) is recognized as an attractive potential hydrogen storage material due to its high hydrogen content and low H_2 release temperature. Hydrogenation of completely decomposed $\text{Mg}(\text{BH}_4)_2$ requires high-temperature, high H_2 pressure, and very long reaction time. Studies show that the partially decomposed $\text{Mg}(\text{BH}_4)_2$ can be hydrogenated in comparatively lower temperatures, pressure, and short reaction time but up to date, the reversible reaction shows only 2.5 wt% of H_2 production which is not sufficient for its practical use. To achieve higher wt% of H_2 it is important to understand the kinetics of the dehydrogenation and rehydrogenation of $\text{Mg}(\text{BH}_4)_2$ reactions and the nature of the reaction intermediates. The latter has been debated for more than 10 years.

In this work, we decomposed $\gamma\text{-Mg}(\text{BH}_4)_2$ at different temperatures between 240-400°C. The composites have been analyzed by using combined thermogravimetric analysis and differential scanning calorimetry (TGA-DSC), X-ray absorption spectroscopy (XAS), and powder X-ray diffraction (PXD) techniques. 11.3 wt% of H_2 desorption at 400°C was observed by gravimetric measurements. PXD showed no crystalline decomposition products when heated between 260-280°C. X-ray absorption near edge structure (XANES) at B K-edge studies was carried out at RGLB, BESSY II, Berlin. The qualitative analysis of the obtained data showed the tetrahedral B co-ordination in the samples decomposed between 240-300 °C and a combination of tetrahedral B with the B-H amorphous species in the reaction products formed in the 300-400°C temperature range. The XANES data also revealed the presence of amorphous boron above 340°C. In this way, this study has provided more insights into the decomposition reaction of $\text{Mg}(\text{BH}_4)_2$. The overall conclusion collected from combined TGA/DSC, PXD, and XAS data analysis have been presented as follows;



Contents:

- 1. Introduction**
 - 1.1. Purpose of the thesis**
 - 1.2. Objectives**
 - 1.3. Background**
- 2. Theory**
 - 2.1. X-rays wave-particle duality**
 - 2.2. X-ray production**
 - 2.2.1. X-ray production in Cathode tube**
 - 2.2.2. X-ray production in Synchrotron**
 - 2.3. X-ray spectroscopy and Interaction of X-rays with matter**
 - 2.4. X-ray absorption spectroscopy (XAS)**
 - 2.4.1 Introduction**
 - 2.4.2 Absorption process**
 - 2.4.3 Quantum mechanical treatment**
 - 2.4.3.1 Free electron approximation**
 - 2.4.3.2 Beyond free-electron approximation**
 - 2.4.4 Absorption edges**
 - 2.4.5 X-ray absorption spectroscopy (XANES)**
 - 2.4.6 Interpretation of XANES**
 - 2.4.7 Measurement modes of XANES**
 - 2.5. X-ray diffraction (XRD)**
- 3. Experiment**
 - 3.1. Experimental details**
 - 3.2. TGA and DSC instrument**
 - 3.3. Glove box**
 - 3.4. Synchrotron Beamline and XANES instrument**
 - 3.4.1 Sample Holders**
 - 3.4.2 XANES instrument**
 - 3.5. X-ray Diffraction instrument**
- 4. Data Processing and analysis**
 - 4.1. TGA-DSC data analysis**
 - 4.2. XRD data analysis**
 - 4.3. XANES data analysis**
- 5. Conclusion and future perspectives**
- 6. References**

1. Introduction

1.1. Purpose of the thesis

The major purpose of this work is to study the partial decomposition reaction of magnesium borohydride as a hydrogen storage material. Mainly to study and analyze the intermediate reaction products when the magnesium borohydride is heated from the temperature between 240-400°C. The experimental analysis methodologies include decomposition and data reduction from combined thermogravimetric analysis and differential scanning calorimetry (TGA-DSC) technique, X-ray absorption spectroscopy (XAS), and the X-ray diffraction (XRD).

1.2. Objectives

Magnesium borohydride ($\text{Mg}(\text{BH}_4)_2$) is One of the interesting materials for hydrogen storage due to its high hydrogen content and the lowest temperature of hydrogen release. In this work, magnesium borohydride will be partially decomposed between 240-400 °C temperature range, and the decomposed reaction product will be studied and analyzed with the thermogravimetric analysis (TGA) and differential scanning calorimetry (DSC) techniques. Furthermore, it will also be studied through the X-ray absorption spectroscopy (XAS) and the powder X-ray diffraction (PXD) techniques in order to identify the intermediate compounds through its weight loss, absorption edge, and the diffraction peaks of the compound formed after the partial decomposition of magnesium borohydride. Through this whole thesis, the following objectives are expected to be fulfilled;

- To carry out experiments and data analysis using TGA-DSC techniques.
- To handle and work well with air-sensitive samples using a glove box.
- To carry out the experiment on X-ray spectroscopy (XAS) and its data analysis.
- To work experimentally on powder X-ray diffraction (PXD) and its data analysis.
- To analyze the data obtained from TGA-DSC, XAS, and PXD using their corresponding software.
- To learn to work in a lab with great responsibility.
- To learn to discuss the results and their consequences to enhance future measurements.
- To learn scientific writing and literature search.

1.3. Background: Magnesium borohydride as a hydrogen storage material

1.3.1. Storing hydrogen in borohydrides

Although the technology of renewable energy utilization such as solar and wind energy, has been researched a lot, instability of the sources for these energies leads to the simultaneous operation of backup power systems. Also, at present, several major industries are currently looking to reduce their dependence on fossil fuels. In the pursuit to find solutions in both of these cases, the hydrogen storage concept surely plays an important role as a renewable source of energy.

Hydrogen is one of the most abundant, but highly flammable elements. It is lightweight, small in size, and a pollution-free energy carrier that is characterized by flexible and efficient energy conversion. However, the low density of hydrogen gas, low temperature of its liquefaction as well as high explosive risk are the major problems of the developments of effective and safe hydrogen storage systems. At present, these problems related to safe and efficient have exceeded the development of hydrogen power engineering and technology. Besides these, all difficulties and the problems with hydrogen storage scientists have been able to discover the methods for hydrogen storage in some physical and

chemical methods including adsorption and absorption. The diagram below shows the recent methods of hydrogen storage in different ways.

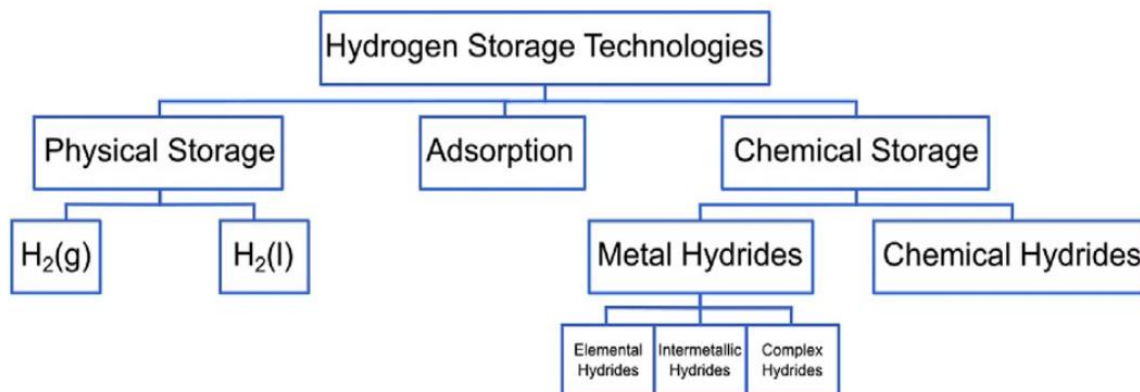


Figure 1.1: The applied categorization of hydrogen storage technology [1]

Hydrogen can be stored by physical methods that contain H_2 molecule which does not react with the storage medium. In the physical method, the hydrogen is stored as a compressed gas in gas cylinders, stationary storage systems including underground reservoirs, hydrogen storage in pipelines, and glass microspheres whereas in liquid form, hydrogen is stored as stationary and mobile cryogenic reservoirs. In the chemical methods, hydrogen storage is done using the physical-chemical process of its interaction with some materials. The methods are characterized by an essential interaction of molecular or atomic hydrogen with the storage environment. These chemical methods include the storage of hydrogen as metal and chemical hydrides. Adsorption and absorption are the material-based hydrogen storage methods. In adsorption, the hydrogen is attached to the surface of material either as hydrogen molecules or as hydrogen atoms. In absorption, the hydrogen is stored within the solids. In absorption, hydrogen is dissociated into H-atoms and then the hydrogen atoms are fused into the solid lattice framework. Absorption in complex hydrides may make it possible to store a larger amount of hydrogen in smaller volumes at low pressure and temperatures close to room temperatures. Finally, hydrogen can be strongly bound within molecular structures as chemical compounds containing hydrogen atoms[1-3]

The table below (Table 1.1) shows the comparison between the different hydrogen storage methods. Among all the methods, the metal hydrides and metal borohydride have high volumetric and gravimetric densities. It is important to recall that the efficiency of hydrogen storage for material depends on several components but usually mainly measured by two parameters, the gravimetric density, and the volumetric density. Gravimetric density referred to the weight % of hydrogen stored the total weight of the system (hydrogen + container) whereas the volumetric density referred to the stored hydrogen mass per unit volume of the system [1, 3].

Practically, the considerable energy losses, expensive storage tanks, and the safety risks are the main challenges associated with the Liquid and pressurized hydrogen tanks [4]. Therefore, almost ten years ago the alkaline and alkaline earth metals borohydrides got the attention as hydrogen storage materials due to their high hydrogen content [5].

| Method | Gravimetric Energy Density (Wt %) | Volumetric Energy Density (MJ/L) | Temperature (K) | Pressure (barg) | Remarks |
|-----------------------|-----------------------------------|----------------------------------|-----------------|-----------------|---|
| Compressed | 5.7 | 4.9 | 293 | 700 | Current industry standard |
| Liquid | 7.5 | 6.4 | 20 | 0 | Boil-off constitutes major disadvantage |
| Cold/ cryo-compressed | 5.4 | 4.0 | 40-80 | 300 | Boil-off constitutes major disadvantage |
| MOF | 4.5 | 7.2 | 78 | 20-100 | Attractive densities only at very low temperatures |
| Carbon nanostructures | 2.0 | 5.0 | 298 | 100 | Volumetric density based on powder density of 2.1 g/mL and 2.0 wt% storage capacity. |
| Metal hydrides | 7.6 | 13.2 | 260-425 | 20 | Requires thermal management system |
| Metal borohydride | 14.9-18.5 | 9.8-17.6 | 130 | 105 | Low temperature, high pressure thermal management required |
| Kubas-type | 10.5 | 23.6 | 293 | 120 | |
| LOHC | 8.5 | 7 | 293 | 0 | Highly endo/exothermal requires processing plant and catalyst. Not suitable for mobility. |
| Chemical | 15.5 | 11.5 | 298 | 10 | Requires SOFC fuel cells |

Table 1.1: The comparison between the different hydrogen methods [2]

In the present work, we mainly focus on magnesium borohydride ($\text{Mg}(\text{BH}_4)_2$) and its characteristics, which made it more interesting hydrogen storage material than other metal borohydrides. Hydrogen storage property of magnesium borohydride could make it a promising and everlasting resource of clean and renewable energy as a replacement for fossil fuel. It can be used in fuel cells and the form of many other energies and can widely use for industrial purposes as well as according to [6, 7], this compound can further lead to magnesium rechargeable batteries.

The table below shows how $\text{Mg}(\text{BH}_4)_2$ stands out among other metal borohydrides from its gravimetric and volumetric densities point of view.

| Hydrogenated form | Dehydrogenated from | Hydrogen capacity | | - ΔH , kJ/mol H ₂ | Decomposition temp. °C | |
|---|--|-------------------|------|---|------------------------|-----|
| | | | | | | |
| LiBH ₄ | LiH + B | 13. | 93 | 75 | 402 | 470 |
| 2 LiBH ₄ + MgH ₂ | 3 LiH + MgB ₂ | 11.4 | | 46 | 225 | 315 |
| 2 LiBH ₄ + Al | 2 LiH + AlB ₂ | 8.6 | | | 188 | |
| 7 LiBH ₄ + 1.75 Mg ₂ Sn + 0.25 Sn | Li ₇ Sn ₂ + 3.2 MgB ₂ | 6.3 | | 46 | 184 | |
| NaBH ₄ | NaH + B | 7.9 | 85.5 | 90 | 609 | 595 |
| 2 NaBH ₄ + MgH ₂ | 3 NaH + MgB ₂ | 7.8 | | 62 | 351 | |
| Be(BH ₄) ₂ | Be + 2B | 20.8 | 126 | 27 | | 123 |
| Mg(BH ₄) ₂ | Mg + 2B | 14.9 | 113 | 40 | | 323 |
| Ca(BH ₄) ₂ | 2/3 CaH ₂ + 1/3 CaB ₆ | 9.7 | 108 | 75.5 | | 360 |
| Ca(BH ₄) ₂ + MgH ₂ | CaH ₂ + MgB ₂ | 8.3 | | | 159 | |
| Zn(BH ₄) ₂ | Zn + 2B* | 8.5 | | | | 85 |
| Al(BH ₄) ₃ | Al + 3B* | 16.9 | 121 | 6 | | 150 |
| Sc(BH ₄) ₃ | ScB ₂ + B (?) | 13.5 | | | | 260 |
| Ti(BH ₄) ₃ | TiB ₂ + B* | 13.1 | | | | 25 |
| Mn(BH ₄) ₂ | Mn + 2B | 9.5 | | | | |
| Zr(BH ₄) ₄ | ZrB ₂ + 2B (?) | 10.7 | 108 | | | 250 |

Table 1.2: Comparison between the gravimetric and volumetric densities of metal hydrides [8].

For any compound to work as hydrogen storage material, besides the gravimetric and volumetric densities they are supposed to have a low temperature of dehydrogenation and moderate or easy reversibility of dehydrogenation, low working pressure, fast kinetics of desorption and absorption and high purity of released and reabsorbed hydrogen gas [4, 8]. Following these facts, among other borohydrides, Mg(BH₄)₂ turns out to be better. From the table above, it can be seen that, among other metal borohydrides, beryllium borohydride and magnesium borohydrides have much better gravimetric and volumetric densities. But beryllium oxide is too toxic for practical applications leaving magnesium borohydride as important hydrogen storage material.

Magnesium borohydride was first synthesized in the 1950s, but the interest in hydrogen energy made it a possible candidate for hydrogen storage [9]. Magnesium borohydride (Mg(BH₄)₂) has the most complex crystal structures and the largest number of phase polymorphs among other borohydrides. Among all known hydrides, some of the polymorphs of Mg(BH₄)₂ contain a noteworthy porosity and also ultra-density with the second-highest volumetric hydrogen [7]. Magnesium borohydride exists in various crystalline forms, as recently discovered and characterized by X-ray and neutron scattering techniques. Among the observed polymorphs of Mg(BH₄)₂, namely α , β , γ and δ -phase, the low-temperature (LT) α -phase and the high-temperature (HT) β -phase are the most commonly investigated for hydrogen storage applications [9]. Many studies have been made to describe the synthesis and the crystal structure of magnesium borohydride which are explained in [7, 9-14].

In the present work, we are going to discuss the γ -Mg(BH₄)₂ phase as this is one that possesses a high porosity of almost 30% of open space in the structure [5]. According to the author of [7] γ -Mg(BH₄)₂ has a cubic crystal structure with space group *Ia-3d* and *I4-3a*, and it is an interesting first example of porous high surface area complex hydride, which can absorb small molecules. The reported values of specific surface area (SSA) for γ -Mg(BH₄)₂ vary greatly between 60 to 1160 m²g⁻¹. This property of γ -Mg(BH₄)₂ eventually can lead to new possible applications where surface effects are important.

γ - $\text{Mg}(\text{BH}_4)_2$ is the interest of the study from the hydrogen storage point of view because it contains 14.9 weight % of hydrogen and has suitable thermodynamics [11] and is more abundant than Li [7]. It contains hydrogen-rich molecular anions $(\text{BH}_4)^-$ and the $(\text{Mg})^{++}$ cations. The gravimetric and volumetric hydrogen densities in this compound are even suitable for the demanding onboard hydrogen storage applications. $\text{Mg}(\text{BH}_4)_2$ can be decomposed between 215-410°C with mainly the release of hydrogen and also reaction is reversible in this temperature range [7]. It has the lowest decomposition temperature among LiBH_4 , $\text{Be}(\text{BH}_4)_2$ and $\text{Mg}(\text{BH}_4)_2$ and all the group I and II borohydrides, and has the modest conditions for partial re-hydrogenation among all borohydrides as demonstrated experimentally on [7]. This is the clear reason why composites based on $\text{Mg}(\text{BH}_4)_2$ are extensively studied fundamentally and are applicable as hydrogen storage materials [15]. Recent studies on $\text{Mg}(\text{BH}_4)_2$ have revealed a more complex multistep decomposition pathway than previously thought, which suggests the formation of B-H amorphous intermediates similar in structure to $\text{MgB}_{12}\text{H}_{12}$. Besides these, studies have also shown an inverse correlation between the electronegativity of the cation and borohydride stability [16].

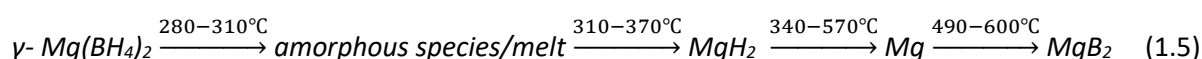
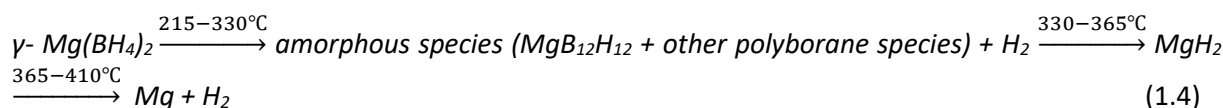
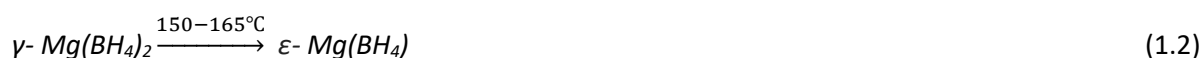
The partial and the complete reversible decomposition of $\text{Mg}(\text{BH}_4)_2$ has been studied using various experimental techniques such as combined thermogravimetric analysis and differential scanning calorimetry (TGA-DSC), X-ray diffractions (XRD), Fourier transform infrared radiation (FTIR), Raman, X-ray absorption spectroscopy (XAS), etc. The studies show that the re-hydrogenation of completely decomposed $\text{Mg}(\text{BH}_4)_2$ requires high temperature, high hydrogen pressure, and long reaction time. However, the partially decomposed $\text{Mg}(\text{BH}_4)_2$ compounds can be re-hydrogenated in much milder conditions [4].

1.3.2 Hydrogen desorption and absorption in $\text{Mg}(\text{BH}_4)_2$

Desorption is the phenomenon where a substance is released from or through a surface of a solid and escape into the surrounding. The process is opposite to sorption which includes adsorption and absorption. These two properties are very important for a compound to work as a hydrogen storage material [4]. Magnesium borohydride is predicted to have favorable thermodynamics which would allow hydrogen desorption at a temperature below 100°C. But, experiments show that the decomposition of $\text{Mg}(\text{BH}_4)_2$ requires at least 200°C. However, the decomposition process of $\text{Mg}(\text{BH}_4)_2$ suggests multiple reaction pathways with the unknown intermediates reaction products. Re-hydrogenation of completely decomposed $\text{Mg}(\text{BH}_4)_2$ is difficult to use for practical purposes as stated earlier but the re-hydrogenation of the intermediate reaction products obtained from the decomposition of γ - $\text{Mg}(\text{BH}_4)_2$ 300°C, it is possible to produce with up to 2.8 wt% of H_2 . During the decomposition of highly crystalline γ - $\text{Mg}(\text{BH}_4)_2$ between 145-215°C, there is a phase transition from $\gamma \rightarrow \epsilon \rightarrow \beta$ and then the decomposition starts. From 215-330°C, the first hydrogen desorption can be observed along with the appearance of amorphous B-H species. In the next stage, the formation of crystalline MgH_2 takes place between 340-355°C which is then followed by the formation of amorphous boron (B) at a temperature between 355-372°C and the decomposition of MgB_2 from 372-420°C. According to the author of [17], there forms an undesirable by-product of diborane detected at temperature 280°C with various amorphous B-H species desorbed H_2 and interacted with each other in multiple steps of complex magnesium borohydride decomposition procedure. The partial decomposition reaction of $\text{Mg}(\text{BH}_4)_2$ in a vacuum, hydrogen backpressure, and Argon (Ar) was studied in [4] which suggests that before the formation of MgB_2 above 280°C, $\text{Mg}(\text{BH}_4)_2$ decomposed to $\text{Mg}_x\text{B}_y\text{H}_z$ amorphous reaction products with up to 6.8 wt% loss and overall reaction pathway of the experiment has been summarised by equation (1.1) given below,



Here are some important steps during the decomposition of γ - $\text{Mg}(\text{BH}_4)_2$ with some maintained reaction environment that is mentioned in [5, 7]

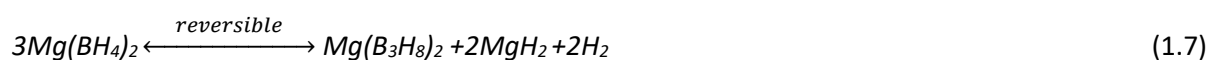


Many experimental reports have shown that in every decomposition step the amorphous intermediate exists and can comprise several competing reactions that can be affected by the reaction conditions and/or the sample history[7, 18-20].

The reactions equations (1.2),(1.3),(1.4) and (1.5) shows the decomposition pathways from temperature 150 °C to 600 °C up to the complete decomposition of γ - $\text{Mg}(\text{BH}_4)_2$. Reaction (1.2) and (1.3) are taken from reference [5] whereas reactions (1.4) and (1.5) are taken from references [7, 18] and [7, 19] respectively. From reaction (1.5) it can be seen that completely decomposed γ - $\text{Mg}(\text{BH}_4)_2$ forms MgB_2 as the final reaction product and needs gaseous reaction with hydrogen for the reversible reaction as given by [15, 19, 21] and as mentioned in reaction (1.6). According to [4] it is possible to reabsorb only about 2.5 H_2 wt% or only 40% of the desorbed amount. The above reactions (1.2) and (1.3) suggests out of the two phases $\text{Mg}(\text{BH}_4)_2$, only one of these is reversible to $\text{Mg}(\text{BH}_4)_2$, so, this can be one of the reasons for incomplete rehydrogenation. Another reason can probably be the formation of a boron-containing intermediate compound in this partial decomposition process is too stable and prevent the complete re-hydrogenation. However, the formation of MgO at the expense of $\text{Mg}(\text{BH}_4)_2$ might have also been responsible for the reduced reVersibility.



But as mentioned in [4], at 200°C γ - $\text{Mg}(\text{BH}_4)_2$ undergoes reversible re-hydrogenation to triborane $\text{Mg}(\text{B}_3\text{H}_8)_2$ according to equation (1.7) and yields 2.5 wt% of H_2 .



Continuous ball milling of magnesium diborane at 400 °C in a hydrogen atmosphere of 950 bar H_2 after 108 hours resulted in 75% of $\text{Mg}(\text{BH}_4)_2$. This product was characterized by TGA-DSC, XRD, IR, and solid-state NMR. Again, the same reaction was carried out at room temperature with 100 bar of H_2 pressure for 100 hours resulted in 50% of $\text{Mg}(\text{BH}_4)_2$.

In summary, the partially decomposed γ - $\text{Mg}(\text{BH}_4)_2$ needs lower temperature and pressure to re-hydrogenate than the completely decomposed one but the hydrogen production during re-hydrogenation is only about 2.5 H_2 wt% which is not sufficient for the hydrogen storage for fuel cells. Its reversible hydrogen storage capacity must start from almost 6 H_2 wt% provided the moderate reaction conditions. Thus, only knowing that the partially decomposed magnesium borohydride can lead to a reversible reaction with less amount of hydrogen production is not sufficient at the moment

rather it has become very important to understand and find out the intermediate amorphous species in order to improve the hydrogen storage property of $\text{Mg}(\text{BH}_4)_2$. Identifying the intermediate species of the reaction will lead the researcher to the different pathways for the improvement of hydrogen storage. For example, by adding additives like transition metal additives to avoid forming the B-H bond during hydrogenation and dehydrogenation of $\text{Mg}(\text{BH}_4)_2$ or preparing reactive hydride composites with $\text{Mg}(\text{BH}_4)_2$ and/or nanoconfinement [7].

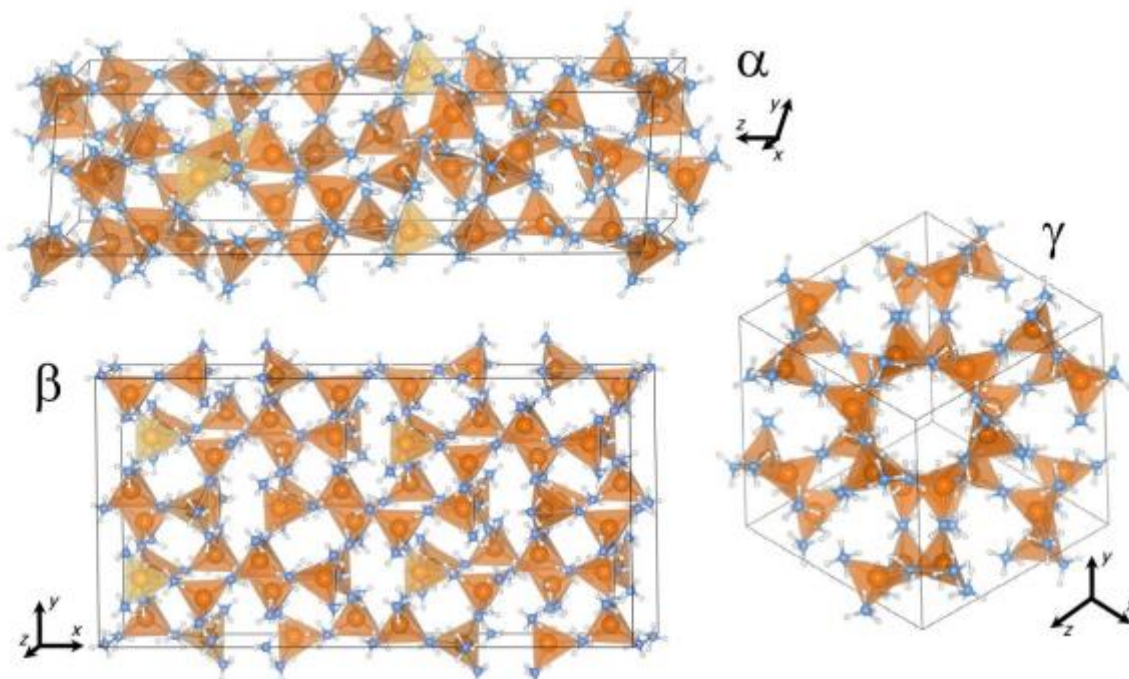


Figure 1.2: Structure of $\alpha\text{-Mg}(\text{BH}_4)_2$, $\beta\text{-Mg}(\text{BH}_4)_2$, and $\gamma\text{-Mg}(\text{BH}_4)_2$ (models obtained using the VESTA program). Magnesium atoms are represented with tetrahedra where each vertex is occupied by a $[\text{BH}_4]^-$ unit and, in all the structures, every vertex is shared between two tetrahedra [20].

So, the main purpose of this work is to study the reaction products of different reaction steps in $\text{Mg}(\text{BH}_4)_2$ decomposition including the intermediate amorphous products formed in the 240–300°C temperature range. For this purpose, several samples were prepared in the lab in different temperatures and the argon flow of 200 ml/min which were then studied by using X-ray absorption spectroscopy (XAS), and laboratory powder X-ray diffraction (PXRD) to characterize the unknown intermediate species.

XAS can find out the composition of these intermediate species by finding out the coordination and the oxidation state of the X-ray absorbing atom in the sample. In the present work, XAS was used to determine the local environment around the boron by obtaining XANES spectra at boron K-edge and this technique was chosen to characterize the partially decomposed amorphous sample because this technique is especially used to probe the amorphous species. Laboratory powder X-ray diffraction (PXRD) was used to identify the presence of crystalline species in the samples and characterize them. As mentioned earlier, the main compounds of interest are amorphous therefore the PXRD was mainly used to determine the composition of starting materials. This method has been traditionally applied for phase identification, quantitative analysis, and the determination of structure imperfections [22].

Samples were prepared using the TGA-DSC instrument. As $\gamma\text{-Mg}(\text{BH}_4)_2$ is a highly air-sensitive sample it was heated up to the desired temperature in the argon (Ar) environment with the Ar flow rate of 200 ml/min. The TGA device measured the change in weight of the substance as the temperature changed and the weight loss curve subsequently gave the information about the change in sample composition, thermal stability, and the kinetic parameters for chemical reactions in the sample. The DSC measurements and the peaks in the heat flow curve gave information about whether the heat is flowing into or out the sample (i.e. endothermic/exothermic reactions). So, the simultaneous TGA-DSC measures both gave the information on heat flow and weight changes in a material as a function of temperature or time in a controlled atmosphere and helped to simplify interpretation of the result. The complementary information obtained from TGA-DSC thus allowed differentiation between endothermic and exothermic events which have no association with weight loss directly but could be because of melting or crystallization and those which involve a weight loss (e.g., degradation) [23].

2. Theory

2.1. X-rays wave-particle duality

X-rays with energies ranging from about 100 eV to 10 MeV (wavelength =10 to 0.01nm) are classified as electromagnetic waves. X-rays are different from the radio waves, light, and gamma rays in wavelength and energy and show wave nature with wavelength ranging from about 10 to 10^{-3} nm. X-rays can be treated both as electromagnetic waves and as particles. According to quantum theory, the electromagnetic wave can be treated as particles called photons or light quanta [24].

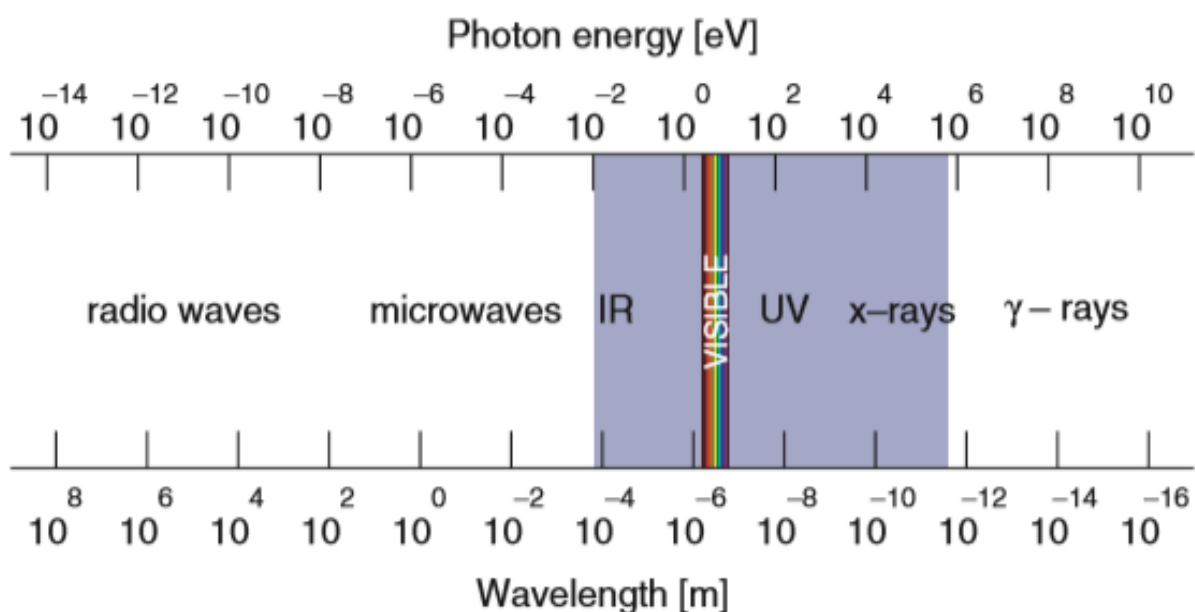


Figure 2.1: The EM spectrum, showing major categories as a function of photon energy in eV and wavelength [25].

Since the X-rays can be treated as electromagnetic waves, they can be explained by classical electromagnetic theory (Maxwell equations). So, as an electromagnetic wave, they show interference (X-ray diffraction), reflection, refraction, and polarization phenomena. As electromagnetic wave X-rays travel through space in a sinusoidal fashion and follows the general relation of a traveling wave as stated below.

Decreasing wavelength (λ) = increasing frequency (f) = increasing energy (E)

X-rays also show particle behavior and their particle behavior can well be explained is by Quantum theory (Schrodinger wave equation). As a particle, they can be produced, show the photoelectric effects and the absorption. The phenomenon is called Compton scattering, which proved that X-rays are particles. Hence, Compton scattering can only be understood by taking X-rays as a particle. [25]

2.2. Production of X-rays

2.2.1. Production of X-rays in Cathode tube:

When a high voltage of several tens of kV is applied between the two electrodes, the high-speed electrons with sufficient kinetic energy are drawn out from the cathode and collide with the anode (metallic target). The electrons rapidly slow down losing their kinetic energy but this kinetic energy losing method for each electron is different, the continuous X-rays with varying wavelengths are generated. When the electron loses all its energy in a single collision, an X-ray with maximum energy is produced with the shortest wavelength. The value of the wavelength limit can be estimated from the accelerating voltage between two electrodes. When the electrons impact the target (the anode), X-rays are produced in two main ways, which is given by:

- Bremsstrahlung:** This form of radiation, 'braking radiation' in German, is explained by the fact that the accelerated electrons, as they hit the anode, are slowed down if they have high energy and the amount of braking (energy) is converted into different forms of radiation. This radiation is diverse and of different wavelengths because, each electron hitting the anode, slows down, and loses its kinetic energy with a different method.
- Characteristic radiation:** This form of energy is produced by the ejection of electrons from either K, L, M etc. orbitals through impacts with other electrons sent from the cathode. Hence a characteristic X-ray emission occurs for specific electron orbits when the energy of incoming electron overcomes the binding energy of the orbital electrons in the target atom [25, 26].

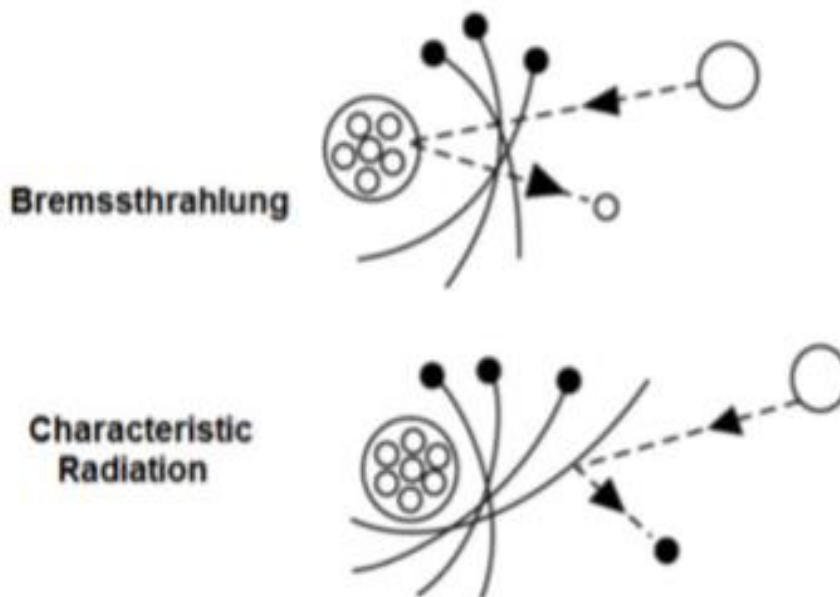


Figure 2.2: The mechanisms of Bremsstrahlung and Characteristic radiation [26].

2.2.2. Production of X-rays in a synchrotron:

Synchrotron radiation is electromagnetic radiation that is emitted when charged particles move at a speed close to the speed of light. In synchrotrons, the moving charged particles are forced to change their direction by using magnetic fields provided by powerful magnets. In nature, synchrotron light can be produced by astronomical objects like crab nebula, which is a supernova remnant in the Taurus constellation. Since the late 1940s synchrotron light has been artificially generated using particle accelerators. Synchrotron radiation covers a wide range of frequency from infrared to the highest-energy X-rays and is characterized by the properties such as high brightness (many orders of magnitude brighter than conventional sources), highly polarization, tunability, collimated beam (almost parallel rays) and concentrated over a small area [27]. This property as a single word can be called brilliance. Another important property is the energy of the electrons within the storage ring which generates the X-rays, which influences the range of photon energies that any one facility can practically cover [25]. The main advantage of synchrotron light source over the cathode tube is that only the single wavelength X-ray is possible to produce once because the anode target material needs to be chosen and kept fixed in the cathode tube, and this is why it is not a tunable resource and also the intensity of the source is less than that of synchrotron [28]

A synchrotron consists of five main components:

1. The electron gun is a source of electron where the electrons are generated by thermionic emission from the hot filament. These electrons are then accelerated using a linear accelerator (linac) at about 100 MeV. A regular supply of electron is required as they are usually being lost in the machine due to collision with residual gas particles in the storage ring.
2. The electrons from the linear accelerator are then injected into the booster ring where they are further accelerated. Then the electrons are periodically injected to the main storage ring so that the specified storage ring current is maintained.
3. The storage ring contains the array of magnets which makes the electrons move in a closed circular path. These are mainly of three types; dipole or bending magnets which cause the electrons to change their path and thereby follow a closed path. Quadrupole magnets are used to focus the electron beam and compensate for Coulomb repulsion between the electrons and sextupole magnets correct for chromatic aberrations that arise from the focusing by quadrupoles. The electrons have K.E measured in GeV and their velocities are highly relativistic (very marginally less than the velocity of light).

The storage ring contains bending magnets (BMs) and the straight sections used for insertion devices (IDs) which generate the most intense synchrotron radiation.

4. Radiofrequency (RF) supply: To supply the electrons just the right amount of extra energy every time they pass through it to replenish the energy loss by the electrons while emission of synchrotron radiation.
5. Beamlines: The beamlines run tangentially to the storage ring, along the axes of the insertion devices and tangentially at bending magnets. Beamlines have three sections; front end, optics hutch, and experimental hutch. The front end monitors the position of the photon beam, filters out the low-energy tail of the synchrotron radiation spectrum if necessary, etc. The photon beam is then normally focused and/or monochromated in the optics hutch. The hutches are shielded using the lead-lined, thick concrete wall to protect users from not only X-rays but also from gamma rays and high-energy neutrons, which can be produced in the storage ring when the relativistic electrons collide with stray gas particles. Such gamma rays penetrate very deeply in the matter, hence effective radiation shields may consist of tens of centimeters of

lead blocks. Experiments in the experimental hutches are therefore performed remotely, from outside the radiation area [25].

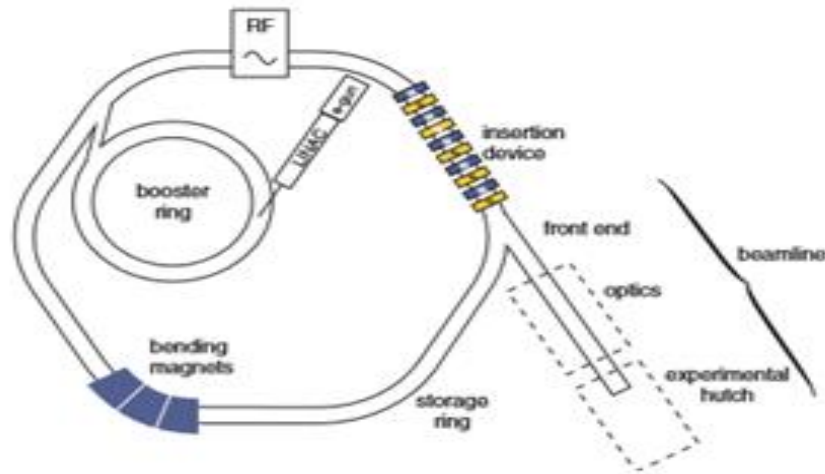


Fig 2.3: Schematic diagram of the most important components of modern synchrotron source [25].

2.3. X-ray spectroscopy and Interaction of X-rays with matter:

X-ray spectroscopy is the study of X-ray electromagnetic radiation and its interaction with matter. It is one of the widely used analytical techniques to study the structure of atoms and molecules. The technique is also employed to obtain information about atoms and molecules as a result of their distinctive spectra [29]. We know that the electromagnetic waves carry energy in terms of waves, so when this energy ($E = h\nu$) carrying waves like X-rays, strikes the particle, they produce some change in the particle. This interaction is studied by a technique called Spectroscopy. Spectroscopy can be carried out in two ways either by absorption or by the emission of electromagnetic waves. When an electromagnetic wave reacts with matter one can obtain either absorption spectrum or emission spectrum, but the spectrum obtained is determined primarily by the atomic or molecular composition of the material. That is why the spectroscopy technique is extensively used to study the internal structure of the material.

From the application point of view, there are mainly following X-ray spectroscopic techniques.

1. X-ray absorption spectroscopy
2. X-ray fluorescent spectroscopy
3. X-ray emission spectroscopy

Several other techniques can be categorized within three of these techniques [25].

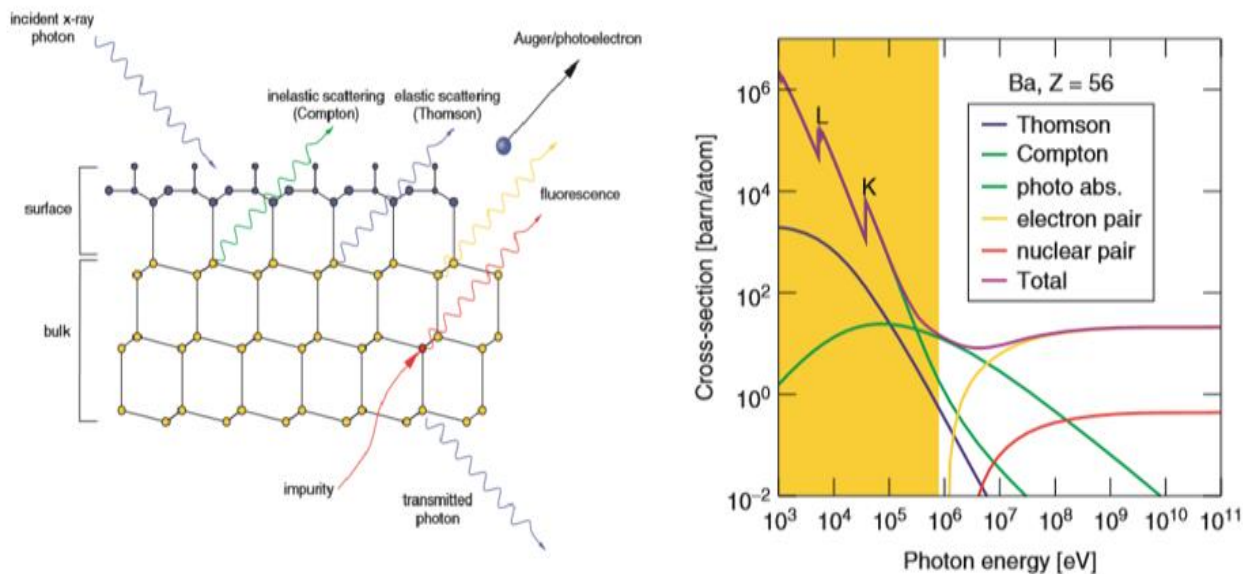


Figure 2.4: (Right) The interaction of X-rays with matter. (Left) The cross-section for various processes involving the interaction of X-rays with the matter for Barium (Ba) [25].

Figure 2.4, (right) shows the possible interaction of X-rays with matter. When the X-rays incident on the matter, the phenomena like refraction, reflection, absorption, scattering (elastic scattering = Thomson scattering and inelastic scattering = Compton scattering), diffraction and fluorescence all are possible processes that can take place. If none of the above takes place, the photon is then transmitted through the sample. But for the applications using synchrotron radiation only photoelectric absorption, elastic and inelastic scattering (which also includes diffraction) are important as shown in Figure 2.3. (left). Figure 2.4, (left) shows the cross-section for five different processes that can take place when X-rays interact with matter. The cross-section is given in the unit of barn which is equal to 10^{-24} cm^2 . The yellow-colored region indicates the upper energy range covered by synchrotron sources up to some MeV. In this range, two processes dominate, namely photoelectric absorption and elastic (Thomson) scattering, although inelastic (Compton) scattering also becomes significant above 30 KeV[25]. Further in this work, X-ray absorption spectroscopy will be discussed as it is the main focus of this work.

2.4. X-ray Absorption Spectroscopy

2.4.1. Introduction

X-ray absorption spectroscopy (XAS) is a photoelectric effect and one of the spectroscopic tools that are widely used in many research labs to study the geometric and electronic structure of the matter. It is useful for probing the internal structure of material nanoparticles. Its use has been increased because of the availability of synchrotron radiation facilities around the world.

When X-ray is scanned through matter, it can ionize the target atom by ejecting electrons from any of the core shells such as K or L or M ... and so on (which depends on the binding energy of each core shells), then there is the sudden increase in absorption cross-section which appear as peaks in the graph and are called absorption edges.

In XAS, the measurements are made by tuning the X-ray energy at and above a selected core-level binding energy of a specific element. The spectra obtained through this process information about the oxidation state and the coordination chemistry of the selected element. In addition, the extended oscillations of the XAS spectra are sensitive to the distances, coordination number, and species of the atoms immediately surrounding the selected element. When the measurements are carried near and at the binding energy (also called the absorption edge) it is called the X-ray absorption near- edge structure (XANES) and measurement above the absorption edge is called extended X-ray fine Structure (EXAFS).

Each atom and ion has a unique internal structure in terms of the number of electrons, binding energies, and atomic environment. This produces a characteristic X-ray absorption spectrum thus allowing for obtaining valuable information on the atomic geometry, electron density, oxidation state, electronic configuration symmetry, coordination number, and interatomic distances of atoms/ions in different molecules and/or compounds [30, 31]. Absorption of X-rays by an atom can be regarded as causing a fluctuation of the electron energy up to a virtual level. When the X-ray hits the target atom, and if the incoming X-rays have energy greater than the binding energy of core electrons, the probability of ejection of core electrons increases and hence the interaction strength or ‘cross-section’ between X-rays and core electrons increases. This interaction between the X-rays and the core electrons are stronger than those between X-rays and valence electrons. Then there is a role of X-ray absorption spectroscopy (XAS) techniques, which are concerned with the change in response of a system as a function of incident photon energy. XAS experiments can mostly be performed at synchrotrons even though the instruments have appeared recently. So, generally in XAS, a core electron is excited to an unfilled valence state and this state can then relax via emission of a photon or maybe radiation less leading to the ejection of photoelectrons, auger electrons or cascade of low energy secondary electrons [25, 32].

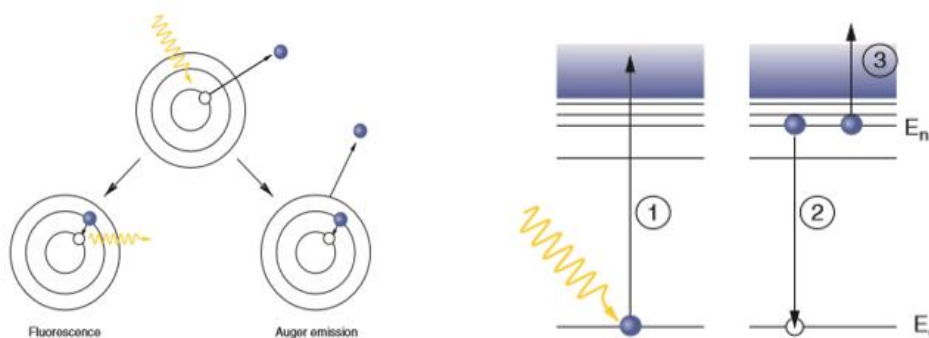


Figure 2.5: The absorption of an X-ray photon proceeds via the ejection of a core electron. This can then be filled by an electron from a shell further out. The excess energy can either be emitted in the form of characteristic X-ray radiation or by the ejection of an Auger electron (left). The three electron process in Auger emission (right) [25].

2.4.2. X-ray Absorption process

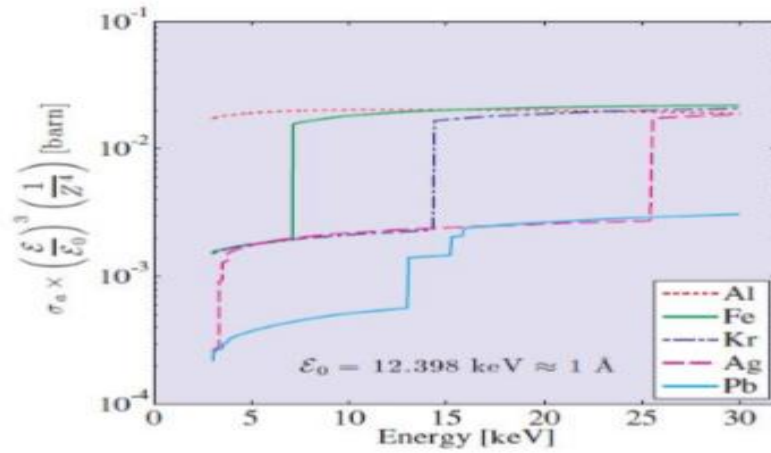
The photoelectric absorption of X-rays is highly dependent on the atomic number Z (approximately to the fourth power) of an atom absorbing the X-rays. The penetrating power of X-ray is dependent on the energy carried by it and also the Z of that atom [33]. The absorbing power of a material is

determined by its absorption coefficient (μ) which describes the exponential drop in intensity of an incident beam passing through a medium. This absorption coefficient of material depends on the type of atoms in the sample, how those atoms are distributed, the nature of their bonding, light polarization, and the wavelength of X-rays. Let us consider the sample of thickness “ d ” in the transmission experiment. If “ I_0 ” denotes the initial intensity of X-ray beam and “ I ” denotes the intensity after transmission through the sample of thickness “ d ”, then the following relation holds,

$$\frac{I}{I_0} = e^{-\mu d} \quad (2.1)$$

Where “ μ ”, is called the linear absorption coefficient, and the above relation is called the “Beer-Lambert” law of liner absorption [25]. The following equation shows the relation of “ μ ” with the absorption cross-section per atom (also called total photon interaction cross-section) denoted by “ σ_a ”,

$$\mu = \left(\frac{\rho_m N_A}{M} \right) \sigma_a \quad (2.2)$$



where N_A , M , and ρ_m are Avogadro’s number, molar mass, and the mass density of an atom.

Figure 2.6: A plot of absorption cross-section vs energy of incident photon for different elements [33, 34]

2.4.3. Quantum Mechanical treatment

The scattering event in quantum mechanics is defined by the time-dependent perturbation theory. The interaction between the incoming beam and the sample is then defined by the Hamiltonian of interaction, H_f , as the transition from an initial state $|i\rangle$ to a final state $\langle f|$. It is also given in first-order perturbation theory by Fermi’s Golden rule, the number of transitions per-second W :

$$W = \frac{2\pi}{\hbar} |M_{if}|^2 \rho(\epsilon_f) \quad (2.3)$$

With the matrix element $M_{if} = \langle i | H_f | f \rangle$ and $\rho(\varepsilon_f)$ being the density of states. The absorption process is not elastic, meaning that the incident photons expels an electron from an atom with binding energy ε_b ,

$$\varepsilon_{pe} = \frac{\hbar^2 p^2}{2m} \quad (2.4)$$

Where this ε_{pe} is the kinetic energy of the photo-electron and is equivalent to the difference between ε and ε_b with ε be the energy of the incident photon. In this case, there are no restrictions over the direction of the wave vector of the photoelectron, \vec{q} and thus, is enough to perform the integration over the entire solid angle of $\Delta\Omega=4\pi$.

$$W_{4\pi} = \int \frac{2\pi}{\hbar} |M_{if}|^2 \rho(\varepsilon_{pe}) \delta(\varepsilon_{pe} - (\varepsilon - \varepsilon_b)) d\varepsilon_{pe} \quad (2.5)$$

The density of states for the photoelectron is evaluated in the same way as for scattering events, using the so-called box normalization [34].

$$\rho(\varepsilon_{pe}) = 2 \left(\frac{V}{8\pi^3} \right) \left(\frac{d\mathbf{q}}{d\varepsilon_{pe}} \right) \quad (2.6)$$

Here factor 2 allows for the two possible spin states of the electron, while the volume element $d\mathbf{q}$ is replaced by $q^2 \sin(\theta) dq d\theta d\phi$. It is now possible to define the absorption cross-section as:

$$\sigma_a = \frac{W_{4\pi}}{\Phi_0} = \frac{2\pi}{\hbar c} \frac{V^2}{4\pi^3} \int |M_{if}|^2 \delta(\varepsilon_{pe} - (\varepsilon - \varepsilon_b)) q^2 \sin(\theta) dq d\theta d\phi \quad (2.7)$$

with $\Phi_0 = c/V$ the incident flux. It also now defines the factor M_{if} (calculation details can be retrieved in book [34]) as:

$$M_{if} = \left\langle f \left| \frac{e}{m} \mathbf{p} \cdot \mathbf{A} \right| i \right\rangle \quad (2.8)$$

Here the terms \mathbf{p} and \mathbf{A} are introduced, which indicate the momentum operator and the vector potential, coming from the interaction Hamiltonian H_f . The expression is then obtained by neglecting the Coulomb interaction between the photo-electron on the positively charged ion left behind. (i.e. free-electron approximation) [33] [35].

2.4.3.1. Free-electron approximation:

It is now briefly reported the derivation of the free-electron approximation for the calculation of the absorption cross-section (full treatment can be read in [34]). The initial state $|i\rangle$ is defined as one photon described by the couple $(\mathbf{k}, \hat{\varepsilon})$ being respectively its wave-vector and its polarization, and one K electron: $|i\rangle = |1\rangle_x |0\rangle_e$. The final state $|f\rangle$ is represented instead by the annihilated photon and the photo-electron expelled by the absorption process: $|f\rangle = |0\rangle_x |1\rangle_e$. It is then found the state for which the electron is free as eigenfunction of \mathbf{p} with eigenvalue $\hbar\mathbf{q}$:

$$M_{if} = \frac{e\hbar}{m} \sqrt{\frac{\hbar}{2\epsilon_0 V \omega}} (\mathbf{q} \cdot \hat{\epsilon}) \int \Psi_{e,f}^* e^{i\mathbf{k} \cdot \mathbf{r}} \Psi_{e,i} d\mathbf{r} \quad (2.9)$$

where r is the position vector of the photo-electron and ψ its wave-function. The square root term is the normalization factor A_0 , which turns out from the quantization of the vector potential \mathbf{A} . It is now considered for the approximation that the initial wave-function of the electron is taken to be that of the 1s bound state, while the final wave-function is of a free electron. These conditions are written respectively as:

$$\Psi_{e,i} = \Psi_{1s}(\mathbf{r}) \quad (2.10)$$

and

$$\Psi_{e,f} = \frac{1}{\sqrt{v}} e^{i\mathbf{q} \cdot \mathbf{r}} \quad (2.11)$$

It is also defined the wave-vector transfer by $\mathbf{Q} = \mathbf{k} - \mathbf{q}$, and its integral as $\phi(\mathbf{Q})$, the Fourier transform of the wave-function of the electron in its initial state. This makes it possible to evaluate the squared matrix element,

$$|M_{if}|^2 = \left(\frac{e\hbar}{m}\right)^2 \frac{\hbar}{2\epsilon_0 V^2 \omega} (q^2 \sin^2 \theta \cos^2 \phi) \phi^2(\mathbf{Q}) \quad (2.11)$$

and thus the absorption cross-section per K electron by substitution of the matrix element in the equation:

$$\sigma_a = \left(\frac{e\hbar}{m}\right)^2 \frac{1}{4\pi^2 \epsilon_0 c \omega} \mathbf{I}_3 \quad (2.13)$$

where \mathbf{I}_3 is a three-dimensional integral, about which definition and evaluation is skipped for convenience (however it can be found in the literature [34]), however, it is found to be reduced to the quantity $\left(\frac{4}{3}\right) \left[\frac{\omega_A^2}{\omega \omega_c}\right]^{5/2}$.

the following quantities are defined as:

- $\hbar\omega_K$: The energy of the absorption edge, proportional to Z^2 for a simple model
- $\hbar\omega_A$: The energy related to K , the inverse length scale of the wave-function Ψ_{1s} , proportional to Z
- $\hbar\omega_c$: The highest characteristic energy, defined as $\hbar\omega_c = 2mc^2$

and hence the final result for the atomic absorption cross-section per atom:

$$\sigma_a = 32\lambda r_0 \left(\frac{4}{3}\right) \left[\frac{\omega_A^2}{\omega \omega_c}\right]^{5/2} ; \text{for } \hbar\omega_K \ll \hbar\omega \ll \hbar\omega_c$$

This makes apparent that the absorption cross-section varies as Z^5 via ω_A , and as $\omega^{-7/2}$ via the factor of $\lambda = 2\pi c/\omega$. This result is slightly different from the experimental findings, summarized in Fig. 2.6.

The reason for this difference is caused by the approximation made for the free-electron, implying the Coulomb interaction between the photo-electron and the positively charged ion to be neglected. However, in this way, it was available to obtain an analytical approximate expression for σ_a [35] [33].

2.4.3.2. Beyond the free-electron approximation:

In this part, we will further show a step in the calculation of the absorption cross-section.

The dimensionless photon energy variable is given by:

$$\xi = \sqrt{\frac{\omega_k}{\omega - \omega_k}} \quad (2.14)$$

and it is conveniently possible to write his result as a correction factor $f(\xi)$ for the absorption cross-section per K electron:

$$\sigma_a = 32\lambda r_0 \left(\frac{4}{3}\right) \left[\frac{\omega_A^2}{\omega \omega_c}\right]^{\frac{5}{2}} f(\xi) \quad (2.15)$$

This correction factor is dependent on both Z and $\hbar\omega$, and its explicit form can be written as:

$$f(\xi) = 2\pi \sqrt{\frac{\omega_k}{\omega}} \left(\frac{e^{-4\xi \operatorname{arccot}\xi}}{1 - e^{-2\pi\xi}}\right) \quad (2.16)$$

it is useful at this point to consider two interesting limits;

1. When the photon energy is greater than the binding energy: $\hbar\omega_k \gg \hbar\omega$ or $\xi \rightarrow 0$, it follows that $f(\xi) \rightarrow 1$.
This returns the same result for the free- electron approximation: If the photon energy is high, so the energy of the photo-electron and it makes a little difference if it is free to move, or it is in a weak attractive field produced by the positive ion.
2. When the photon energy is approaching to threshold energy: $\hbar\omega \rightarrow \hbar\omega^+$, $\xi \rightarrow \infty$, it follows that $f(\xi) \rightarrow \frac{2\pi}{e^4}$

At the threshold energy, there is thus a discontinuous jump of :

$$\sigma_a = 32\lambda r_0 \left(\frac{4}{3}\right) \left[\frac{\omega_A^2}{\omega \omega_c}\right]^{\frac{5}{2}} \left(\frac{2\pi}{e^4}\right) \quad (2.17)$$

To calculate the values for ω_A and ω_k , needed for the evaluation of the energy dependence and the step height in σ_a at the K-edge, it uses the approach of the hydrogen atom. In this way, the K shell ionization of an atom with Z electrons is approximately the binding energy of the hydrogen atom times Z^2 : $\hbar\omega_k = \frac{Z^2 e^2}{\pi a_0 \epsilon_0^2}$ while $\hbar\omega_A = \frac{Z\hbar c}{a_0}$.

It is, therefore, possible to write the edge jump per K electrons as:

$$\sigma_a(\lambda_k) \simeq \left(\frac{256\pi}{3e^4}\right) \lambda_k r_0 \quad (2.18)$$

and energy dependence as:

$$\sigma_a \simeq 32\lambda r_0 \left(\frac{4}{3}\right) \left[\frac{\omega_k}{\omega}\right]^{\frac{5}{4}} \left(\frac{2\pi}{e^4}\right) \quad (2.19)$$

the results that are shown in the last two (write the name of the equations) are proven to be reliable, as compared to recent experiments and more detailed and refined frameworks.

2.4.4. Absorption edges

When the X-rays are scanned through the target material, one can see the abrupt increase in the absorption cross-sections in the particular energy ranges of an incident photon. This happens when the energy of a scanned X-ray corresponds to the binding energy of the core-shell electrons and the corresponding peaks are said as K-edge, L-edge, M-edge, and so on, with each edge representing the different core- electron binding energy. The table below shows the absorption edges and the orbital electrons responsible for it.

| Absorption edges | Electron Transition states | | | |
|------------------|----------------------------|----|----|----|
| K-edge | 1s | | | |
| L- edge | 2s | 2p | | |
| M- edge | 3s | 3p | 3d | |
| N- edge | 4s | 4p | 4d | 4f |

Table2.1: Absorption edges and corresponding electronic transitions

Figure 2.7 shows three major transitions in Pb (K, L, and M edges), corresponding to the excitation of an electron from $n= 1, 2,$ and 3 shells, respectively. At higher resolution, both the L and M edges are split [30]. When there occurs the resonance of X-ray photon energy with the ionization threshold of K or 1s state, this results in K-edge and does not have any sub edges (which L or M can have). The reason for not seeing sub edges in K-edge is that the orbital angular momentum (l) for K orbit is zero and therefore there can be no coupling, which is possible in L or M edges where the orbital angular momentum is not zero [25].

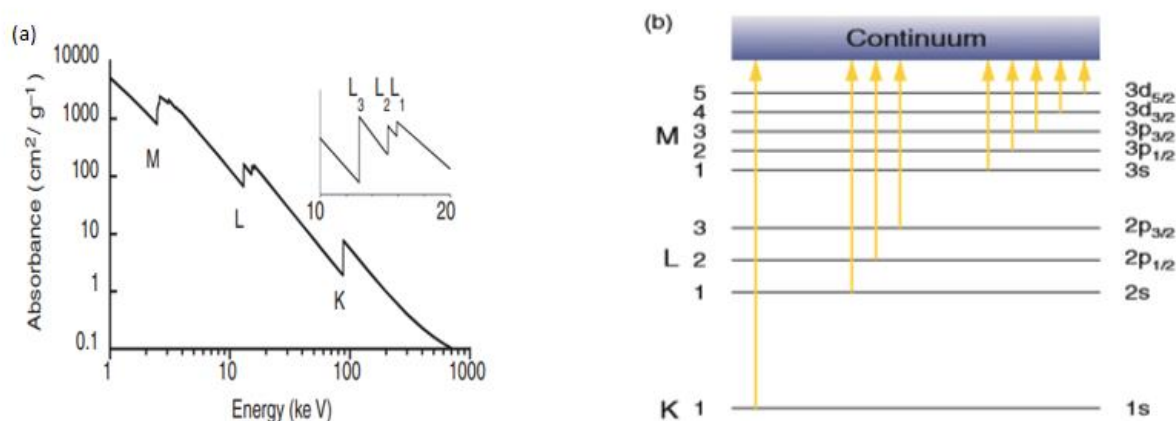


Figure 2.7: (a)Low-resolution X-ray absorption spectrum for Pb [30]. (b) Atomic orbital labeling [25].

Thus, X-ray absorption spectroscopy (XAS) is the measurement of the X-ray absorption cross-section in the vicinity of one or more absorbing edges. X-ray absorption edge is a very- important part of the X-ray absorption spectrum because it is not only the discontinuous increase in absorption, but it shows the significant structure both in the immediate vicinity of the edge jump (XANES) and well above the edge (EXAFS) which can extend up to more than 1,000 eV. The absorption edge region, which is within

the 50 eV of the main edge, is divided into three sub-regions namely, the pre-edge region, the main edge region, and the post-edge region. Before the main edge, sometimes it is possible to observe some small peaks which are called pre-edge structures. The main region where the abrupt increase in the cross-section is observed is called the absorption edge and the immediate region after the main edge which extends up to few eV, having very little fluctuation in absorption cross-section is the post-edge region. The Post-edge region is the region before the EXAFS region.

2.4.5. XANES

X-ray absorption near-edge structure (XANES) is a type of absorption spectroscopy that indicates the features in the XAS spectra of compounds due to photoabsorption cross-section for the electronic transition from the atomic core level to final states, in the vicinity of the absorption edge of an atom. Most importantly, the ability to make qualitative fingerprint-like comparisons of XANES spectra is making it a very useful tool to find out the information about the unknown substance. If a representative library of reference spectra is available, spectral matching can be used to identify an unknown. Beyond this qualitative application, there are three main ways in which XANES spectra are used: to determine the oxidation state, to deduce three-dimensional structure, and as a probe of electronic structure [30] around the X-ray absorbing atom. This technique uses synchrotron radiation to provide the spectra containing valuable information. In XANES, a photon is absorbed, and an electron is excited from a core state to an empty state. To excite an electron in a given core-level, the photon energy has to be equal or higher than the binding energy of this core-level. This gives rise to the opening of a new absorption channel when the photon energy is scanned. The energy of an absorption edge, therefore, corresponds to the core-level energy, which is the characteristic for each element, making XANES an element-selective technique.

In XANES, X-ray ejects the core electron to the empty shell of an atom and generates the core hole and the process is dominated by Fermi- Golden rule which gives the probability of transitioning from initial states to the final states of the ejected photoelectron. When the dipole approximation is taken into account, it applies the selection rules as,

$$\Delta l = \pm 1$$

where l is the orbital angular momentum quantum number and the selection rule states that only the following transition is available giving rise to the specific edges.

1s → K-edge

2s, 2p → L-edges

3s, 3p, 3d → M-edges

4s, 4p, 4d, 4f → N-edges

One can also have quadrupole transition ($l = \pm 2$) but they are very weak and are not significant [36].

The absorption edge is more complex than just an abrupt increase in absorption. There are weak transitions below the absorption edge in the pre-edge region. The pre-edge is strongly affected by the bond lengths of the molecules because of exponential decay of wavefunctions, and the edge is to indicate the ionization energy of the core hole.

Physically during experiments, when the energy of X-ray matches or exceeds the binding energy of core electrons, those electrons get ejected or occupy unfilled valence shell and the vacant space of

these electrons are recovered either by photoemission or by the emission of auger electrons and hence electric current generated from these auger electrons are measured as a function of incident energy.

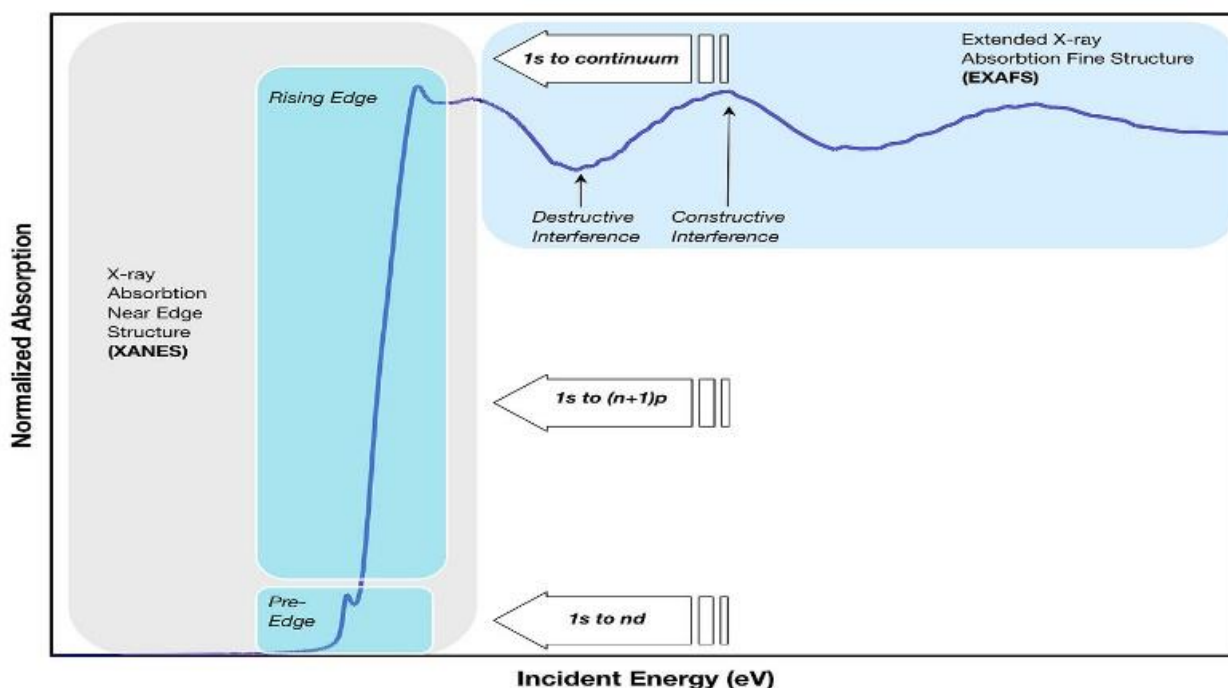


Figure 2.8: XAS spectrum showing important regions of XANES, namely pre-edge, main-edge, post-edge, and the EXAFS region [37]

The pre-edge region in XANES spectra is because of the electronic transitions to the empty bound state (transitions probability controlled by dipolar selection rules). For example, $1s \rightarrow 3d$ or $1s \rightarrow 4p$ is the transitions in 1st transition series metals. This region contains information about the local coordination environment around the absorbing atom, but this information is dependent on the oxidation state and the bonding of the compound in the study. The main edge peak defines the ionization threshold to continuum states and gives the information about the main edge shifts to higher energy with increasing oxidation state.

2.4.6. Interpretation of XANES

1. The sensitivity of XANES to Oxidation state

Edge spectra even though frequently have unresolved transitions superimposed on the rising edge, have proven extremely useful in determining the oxidation state of the absorber. This may be explained by using an electrostatic model since atoms with a higher oxidation state should have a higher charge, thus requires an energetic X-ray to eject the electron from its core. An alternative interpretation treats the edge features as “continuum resonance”. A continuum resonance involves the excitation of a core electron into the state above the continuum that has a finite lifetime. This phenomenon correlates the edge energy and oxidation state of the compound of interest and hence is widely used in coordination chemistry.

2. Bound state transition in XANES

The weak pre-edge transitions generally arise from bound state transitions. For the K edge of a first-row transition metal, these structures arise from $1s \rightarrow 3d$ transitions and are observed for every metal that has an open 3d shell. Although the $1s \rightarrow 3d$ transition is forbidden by dipole selection rules, it is nevertheless observed due both to $3d+4p$ mixing and to direct quadrupolar coupling.

3. Applications of XANES to Coordination Chemistry:

Data analysis and measurements for XANES spectra are much easier than EXAFS spectra since even weak transitions are considerably more intense than EXAFS oscillations. Secondly, XANES spectra can often be treated spectroscopically, that is, the individual spectral features can be correlated to the specific features in the electronic structure which is not possible in the case of EXAFS.

Even though, XANES region has to be scanned during the measurement of EXAFS, relatively little use has been made of XANES except for the qualitative comparisons of an unknown spectrum to reference spectra. Very limited attention has been given to the quantitative analysis of XANES spectra despite the fact that the XANES spectra are difficult to be interpreted when the multiple scattering has to be taken into account. With the development of new theoretical and computational approaches to XANES, the utility of XANES for investigating coordination complexes is likely to increase.

2.5. Measurement modes of XANES:

Generally, the XANES measurements can be carried out in three different modes. They are ;

- a. Transmission mode
- b. Total electron yield (TEY)
- c. Total Fluorescence yield (TFY)

The table below shows the characteristics of a sample to be used in different measurement modes.

| Characteristics of the sample | Transmission mode | Total electron yield | Fluorescence yield |
|-------------------------------|-------------------|----------------------|--------------------|
| Sample thickness | Thin | Thick/ Any | Thick/ Any |
| Background | High | Moderate | Low |
| sensitivity | Bulk | Surface | Bulk |
| Sample concentration | High | High | Low |

Table 2.2: Experimental considerations for different measurement techniques of XAS [38]

Transmission mode involves passing X-rays through the sample and comparing the incident to the transmitted intensities according to the equation(2.1). Transmission measurements may be performed on any type of sample (solid, liquid, gas) provided the thickness and density are controllable. This method is generally suitable for the hard X-ray range [39]. In the soft X-ray range, the transmission mode becomes difficult because of the soft X-ray being used the absorption becomes quite large and the samples must be extremely thin to be penetrated. Fluorescent yield mode is used when the element of interest is present in the dilute condition. However, when used for concentrated samples, a phenomenon called "self-absorption" can

lower the apparent absorption coefficient at high levels of absorption due to non-negligible reduction in the penetration depth as the absorptivity increases, and re-absorption of the fluorescence photons by the same species before the photons can leave the sample.

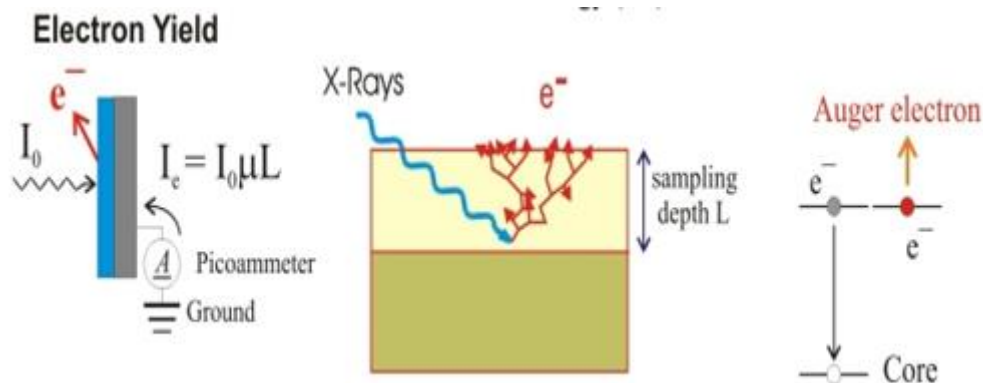


Figure 2.9: Electron yield mode of XAS [40] [41]

The total electron yield (TEY) mode is better when concentrated or thick samples are used where the surface sensitivity is required [39]. As the sample absorbs X-rays, it results in the emission of electrons proportional to the absorption coefficient, from both photoelectrons and Auger electrons. Photoelectrons are those that are ejected from core orbitals and Auger electrons are emitted as part of the relaxation process as a higher-orbital electron fills the hole left behind by the photoelectron. The collection of all produced electrons is called the total electron yield. When the intensity of emitted primary electrons is directly used to measure the X-ray absorption processes, it is called the Auger electron yield which is highly surface sensitive. As the primary Auger electrons leave the sample, they create scattered secondary electrons which dominate the total electron yield (TEY) intensity.

For this experiment, TEY in the soft X-ray range between (160-260 eV) has been chosen to analyze the B K-edge edge of the sample as the sample is concentrated as well as TEY mode is depth sensitive and offers the ability to separately probe the surface phenomena [42]. Thus, the total electron yield (TEY) mode will be discussed in the section below [38].

Figure 2.10 below, shows the experimental arrangement for TEY mode of data collection of XANES. The TEY process involves the collection of scattered electrons from the sampling depth. Electrons created deeper in the sample lose too much energy to overcome the work function of the sample and therefore do not contribute to TEY. The sampling depth in TEY measurements is generally a few nanometers, which is 5nm for B, while it is often less than 1nm for AEY measurements[40, 41].

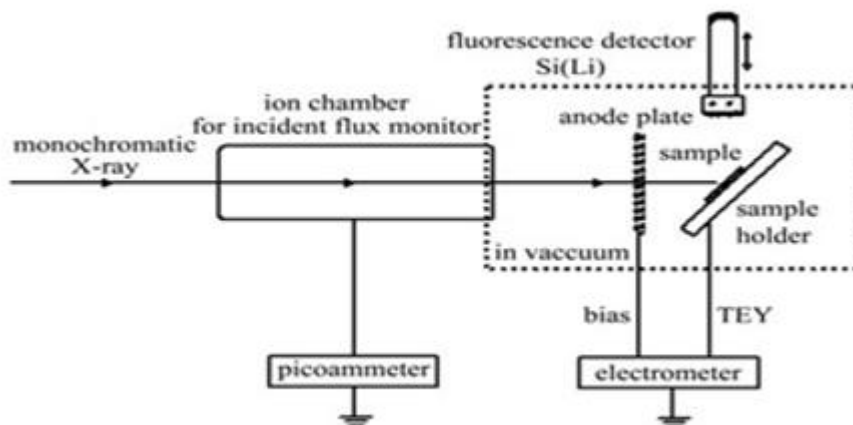


Figure 2.10: The schematic presentation of TEY [39]

2.5. X-ray Diffraction

Diffraction of light occurs whenever the wave motion encounters a set of regularly spaced scattering objects, provided that the wavelength of the wave motion is of the same order of magnitude as the repeat distance between the scattering centers. Most materials are made up of many small crystals and each of these crystals is composed up of a regular arrangement of atoms or molecules. This kind of arrangement of atoms/ molecules forms equidistant planes in the crystal. Von Laue reasoned that, if crystals were composed of regularly spaced atoms which might act as scattering centers for X-rays, and if X-rays were electromagnetic waves with the repeating periods called wavelength of about equal to the interatomic distance in crystals, then it should be possible to diffract X-rays by means of crystals. Two English physicists, W.H. Bragg and his son W.L. Bragg analyzed Laue's experiment and was able to express the necessary conditions for crystal diffraction.

In a crystal, repeating arrangement of the atoms form distinct planes separated by a specific distance. When an X-ray encounters the crystal planes with an atom, its energy is absorbed by electrons. Since this energy is not enough energy for the electrons to knock out from their orbit, this energy must be released in the form of a new X-ray with the same energy as the original. This process is called elastic scattering. Bragg's law gives the condition for constructive or destructive interference of these scattered waves. According to Bragg's law, when the two or more scattered rays are in phase meaning that the next wave/waves must travel the whole number of wavelengths for the constructive interference. In other words, the path difference between two scattered waves should be the integral multiple of the wavelength of incident X-rays for constructive interference which is when one can observe the diffraction. If the two scattered waves are out of phase, the signal will be destroyed and hence it is called destructive interference, consequently one does not observe the diffraction. Mathematically the Bragg's law is written as;

$$2d \sin\theta = n\lambda \quad (2.20)$$

Where 'd' is the interatomic/ interplanar distance. 'λ' is the wavelength of the light used and 'n' is the number of wavelengths as a path difference between two scattered waves and this is also called the order of diffraction. '2θ' is called the angle of diffraction which is the angle between the direction of the incident wave and the scattered wave direction. The exact angle at which the diffraction occurs

can be calculated with the help of the interatomic distance (belongs to the crystal structure) and the wavelength of the X-ray used.

Theoretically, diffraction intensities are calculated by using the idea of “structure factor” (F_{hkl}) where (hkl) refers to the miller indices of the plane which scatters the X-rays. The intensity (I) of diffraction is proportional to the square of the structure factor as;

$$I \sim |F| \cdot |F^*| \quad (2.21)$$

The structure factor is determined by the atomic position and atomic scattering factor (f), unique for every atom. So even if Bragg’s law shows the particular diffraction direction (2θ) is allowed, the structure factor can be “zero” and hence no peak will be observed. The information about the systematic absences of the hkl diffraction peaks due to specific Bravais lattice and atomic coordinates are provided by the diffraction selection rules. Not all the hkl peaks are allowed by the diffraction selection rules which are present in the diffraction pattern some peaks can be absent due to the nature of atoms and atomic scattering factors canceling each other. The relationship between Bravais lattice and reflections necessarily absent can be found systematically in [24].

XRD technique at present can be used for a variety of materials ranging from single crystal to polycrystals and mixtures of powder and even the randomly oriented amorphous materials. In this work, we are going to use the powder X-ray diffraction technique to find out if any crystalline structure exists in the intermediate unknown species obtained from partially decomposed γ - $Mg(BH_4)_2$ in different temperatures by using the TGA/DSC instrument [24, 43].

3.Experiments

Commercial gamma magnesium borohydride (γ - $Mg(BH_4)_2$) (Sigma-Aldrich, 95%) was used to prepare the samples.

Amorphous boron powder (B) (purity >95%, sigma-Aldrich), boric anhydride (B_2O_3 ,) (>99.98, Sigma-Aldrich), magnesium boride powder (MgB_2) (>99%, Mesh), boric acid (H_3BO_3) (ACS reagent, >99.5%, Sigma-Aldrich) ,and lithium borohydride ($LiBH_4$) (>90%, Sigma-Aldrich) were used as references.

3.1. Experimental details

All the data reported here for thermogravimetric analysis (TGA) and differential scanning calorimetry (DSC) and the powder X-ray diffraction (PXD) are collected research laboratory situated at the University of Stavanger, and X-ray absorption spectroscopy (XAS) data were collected at RGLB beamline at BESSY II synchrotron radiation facility, Berlin Germany. All the samples were prepared by heating fresh γ - $Mg(BH_4)_2$ in different decomposition temperatures between 240-400°C in TGA-DSC 3+ instrument. As γ - $Mg(BH_4)_2$ is air sensitive, most of the part of this experiment was carried out in a protective Ar atmosphere inside the glove box. XAS data in the analytical chamber in the beamline were collected in a vacuum even though the samples were prepared in Ar.

3.2.TGA-DSC instrument

To prepare air-sensitive samples at different temperatures, the combined TGA-DSC measurements were carried out using the TGA-DSC 3+ instrument from METTLER TOLEDO. This is a part of the METTER TOLEDO STAR^e system. TGA is a technique that is frequently used for thermal analysis of the samples at different temperatures. Its main use is to characterize the materials by measuring their mass as a function of temperature or time. From TGA generally the composition, purity, decomposition reaction, decomposition temperature, absorbed moisture content, etc. of a sample are measured. TGA is often

used with DSC (differential scanning calorimetry) because these two techniques together provide valuable information for the interpretation of the thermal analysis experiment [44] .

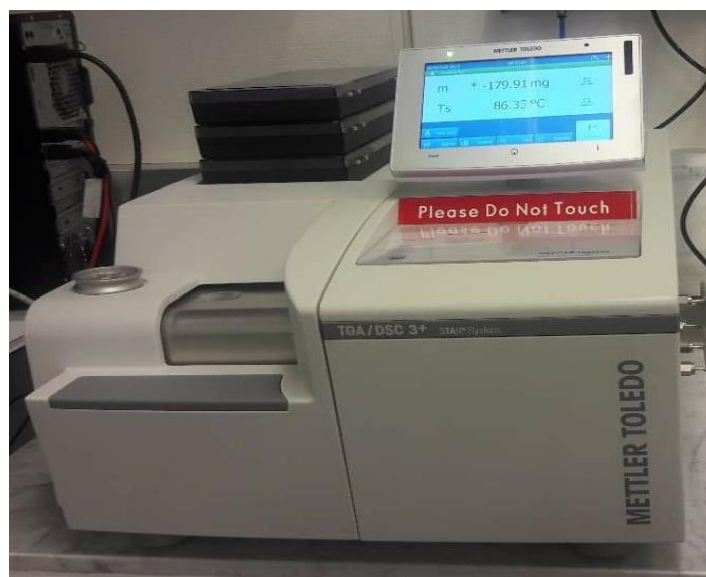


Figure 3.1: TGA-DCS 3+ METTLER TOLEDO situated at UiS research lab

The crucible used for the partial decomposition of γ - $\text{Mg}(\text{BH}_4)_2$ was the alumina (Al_2O_3) crucible of size of 70 μl . For this experiment, the TGA/DSC measurements were conducted dynamically in a linear temperature ramp and isothermally. The temperature ramps are used to investigate the temperature-dependent process such as loss of moisture, composition, and chemical reactions. Isothermal measurements are used to determine the amount of the gaseous reaction products released from the sample. The inert atmosphere was used by making the use of Argon flow at a rate of 200 ml per min throughout the experiment. The simultaneously measured DSC heat flow signal then recorded the exothermic and endothermic events such as phase transitions and decomposition of chemical reactions etc.

In order to heat the samples in TGA/DSC, the first step was to create the methods with all required conditions at which the samples needed to be measured should be set up in the METTLER software. To get the blank measurement as a background (which should be subtracted with the measurement with sample), the experiment then should run in the same set up with empty crucible. Once the blank measurement was obtained, the measurement should then taken by using the same method which then gives the final measurement and the graph for TGA/DSC curves with the subtracted background.

In order to take the measurements with samples, firstly, the mass of the empty crucible should be taken and tared in the in-built balance of the instrument. The next step is to fill the samples in the same crucible which was done inside the glove box filled with Ar. Finally, the real measurement of the sample was run with the already set up parameters, in which the blank curve was run previously. All the samples were decomposed at Ar flow rate of 200 ml per minute inside the TGA/DSC instrument.

3.3. Glove box

For handling the air-sensitive sample, the **MBraun** glove box was used. All the sample preparation was done inside the glove box with a continuously purified and protected Argon (Ar) atmosphere. During the sample handling inside the glove box, water molecules level was always below 0.5 ppm and the oxygen molecules level was below 8 ppm (here ppm is abbreviated for parts per million).

The main parts of the glove box:

- a. The main box to work inside.
- b. A pair of rubber glove
- c. Small antechamber
- d. Large antechamber

Most of the time, the small antechamber is used as it has small volume, it will be easy to evacuate and refill with the inert gas. Every time the glove box is used one must check the level of water (H₂O), oxygen (O₂), and the gas pressure inside the glove box on the screen. This screen works as a control unit of the glove box where the levels for the water or oxygen or other components are shown in the unit of ppm (parts per million) and the used gas pressure inside the box is measured in millibar (mbar). While working on glove box one should always be very careful not to cut or damage the rubber glove. While taking things inside the glove box from outside, one must first open the outer door of one of the antechambers and put everything inside the chamber, then the chamber needs to be flushed with argon/inert gas for a couple of times. For this experiment argon was flushed the always at least 3 times. Flushing is generally done to remove the moisture and other components from the items that is being taken inside the glove box and it is done by evacuating and refilling the chamber by argon gas. One must refill the chamber with argon at the end of the flushing process to open the door of the antechamber from inside the glove box and prepare the necessary sample. To maintain the proper working atmosphere inside the glove box is very important. For this purpose, one needs to decide which substance is to keep inside the glove box and which not. This is an isolation device so; it never should be open to the air. Ante chambers should be under a dynamic vacuum to minimize the solvent vaporization inside the glove box.

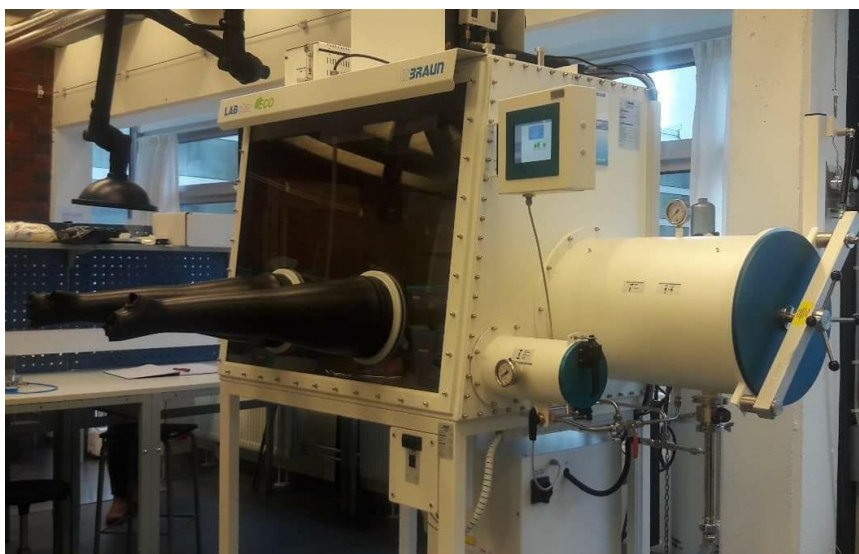


Figure 3.2: Glove box used for the experiment situated at UiS research lab

Problems and precaution while using the glove box

Working correctly on a glove box was the most crucial but tough part of the experiment. It is most important to use the glove box with careful steps, otherwise, the air-sensitive sample gets contaminated with air or water and can destroy. Sometimes it is possible to make mistakes by forgetting to flush the antechamber with argon after putting the items that are being taken inside from outside. At that time, the H_2O and the O_2 level increase abruptly and can reach up to several hundred ppm and even have a chance to contaminate the samples that are inside the glove-box. So, at that time it is important to re-circulate the argon or the inert gas inside the glove-box step by step as quickly as possible by throwing the air-contaminated gas outside and putting in the pure argon inside the glove-box. This must be done until the O_2 and H_2O levels reach at least <10 ppm. Thus, leaving the sample's lead open even inside the glove-box is never a good idea.

3.4 Synchrotron Beamline and XANES instrumentation

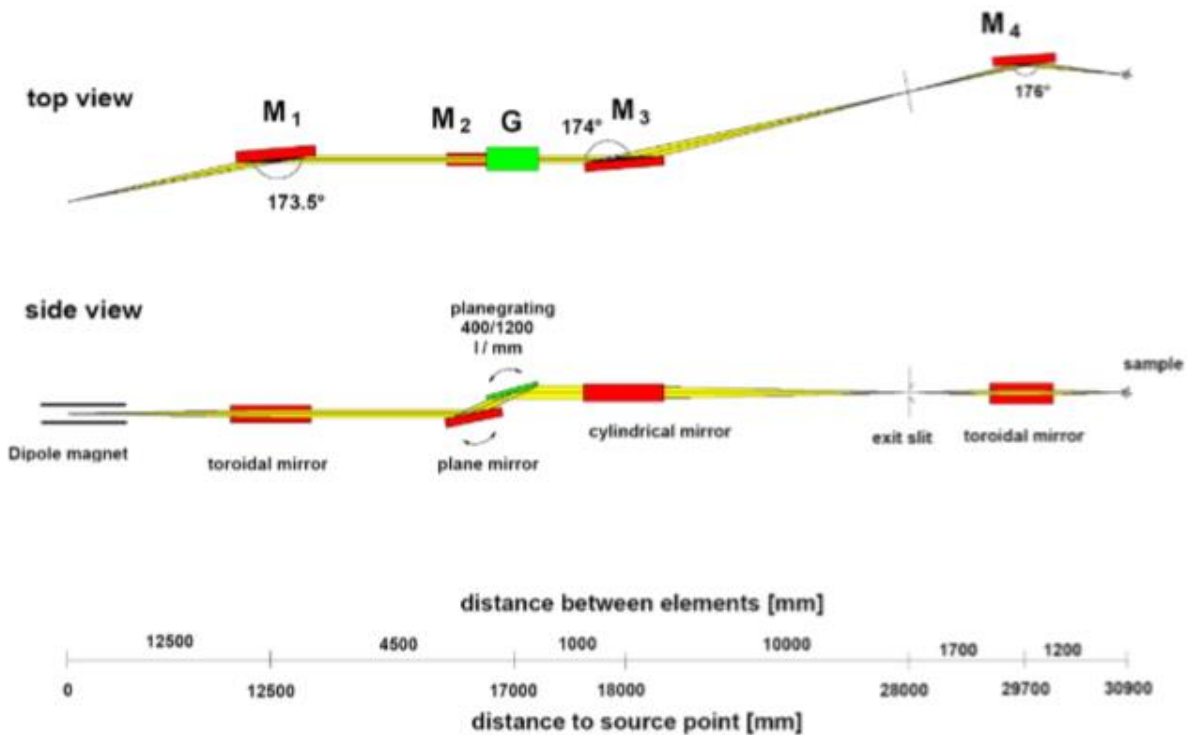


Figure 3.3: Schematic presentation of Russian- German Beamline (RGLB) at BESSY II[45]

The Russian–German beamline at the dipole magnet D16-1A of the Berliner Elektronen speicherring für Synchrotronstrahlung (BESSY) is a central part of the hardware of the Russian-German laboratory at BESSY II. RGLB dipole is dedicated to high-resolution photoemission and photoabsorption research in the photon-energy region between 30 and 1500 eV. This is a plane grating monochromator beamline. This beamline works under up to 2.5×10^{11} photons/100mA of flux and provided with horizontal polarization. It works under the temperature range of 110-295 K and UHV (ultrahigh vacuum) pressure [45].

To obtain the boron K-edge spectra, the surface-sensitive Total electron yield (TEY) mode was used and the TEY signals were collected via drainage current from the experimental sample.

3.4.1. Sample holders

For the experiment in RGLB beamline, XAS experiment was checked by keeping the samples in three different types of sample holders as shown in the figure below but the final data collection was done using the indium tape on the top of stainless- steel which is shown in picture number b) of figure 3.4.



Figure 3.4: Three different types of sample holders for XAS experiment. The first picture with indium tape on the top of the stainless-steel sample holder and the stainless-steel pallet over it (a). The second picture with copper tape on the top of the stainless-steel sample holder (b). The third picture with indium tape on the top of the stainless-steel sample holder (c).

3.4.2. XANES instrument

The samples were prepared in the glove box with great precautions. The sample holders were then transferred to the main XANES instrument by perfectly setting up the required pressure and temperature in the chambers of XAS instrument. After the samples were loaded to the main analytical chamber, the sample holder had to be perfectly positioned so that the samples got hit by the X-ray flux in the desired position of the sample. For this purpose, the X, Y, and Z positions as well as the polar and the azimuthal angles of the sample holder were perfectly adjusted. Then after, setting up the required energy range of the X-ray flux, the experiment was then started when the X-ray flux started falling upon the sample and corresponding readings and the graph started being seen on the computer screen. Once the scanning of the targeted sample by the X-ray is finished, the file should be saved, and the other scan should be started. The measurements were performed in an ultra-high vacuum, the samples were located at 45° to the X-ray beam.

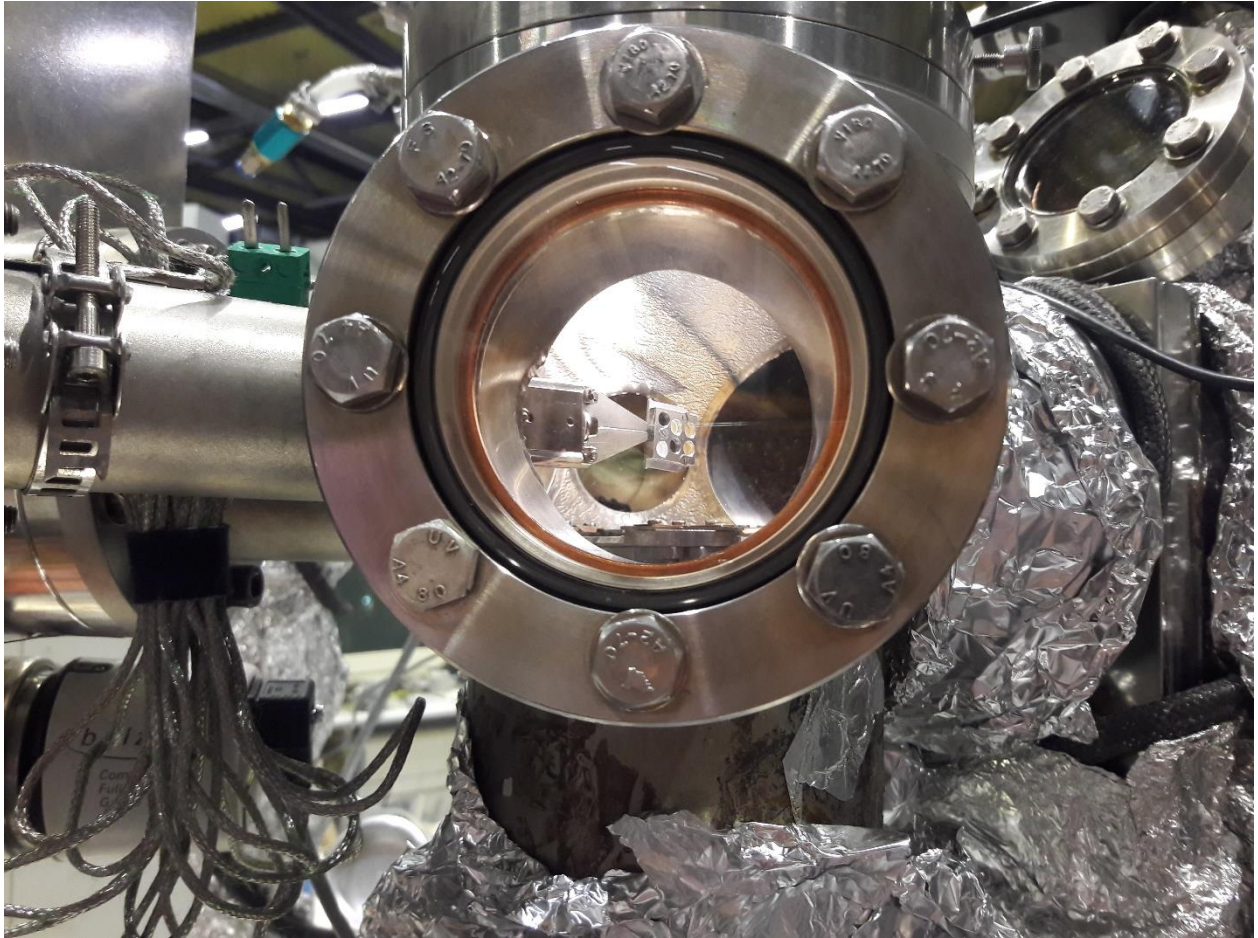


Figure 3.5: The Main analytical chamber (inside the glass window) for performing XAS experiment in RGBL, BESSY II, Berlin. The stainless-steel pallet with six different samples is being treated with X-ray.

3.5. XRD instrument

For this experiment, a D8 Advance diffractometer from Bruker from the Uis Materials' Science laboratory, was used. D8 Advance diffractometer uses copper X-ray source which produces X-rays of wavelength (λ) 1.5418 Å.

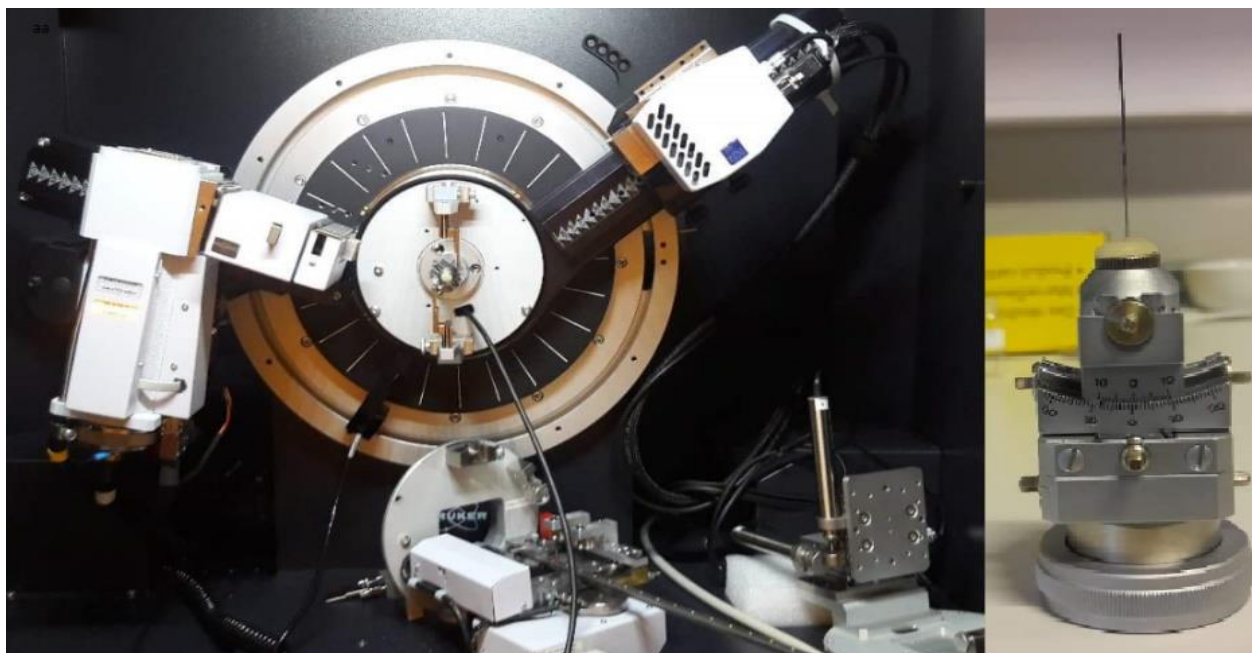


Figure 3.6: Bruker's D8 Advance diffractometer situated in the UiS Materials' Science lab with the sample at the center (left), Goniometer to mount the capillary filled with sample (right).

X-rays produced by heating the filament in cathode ray tube were accelerated towards a target by applying a 40Kv voltage and 25mA current. During the experiments, electrons accelerated with 40Kv bombarded the target material and produced the characteristics X-rays. This X-ray can contain different types of spectra, among all, K_{α} and K_{β} are well-known. A monochromator is used to produce a monochromatic X-ray which is necessary for diffraction. The monochromatic light is then made to fall on a sample by selecting a certain range of angles between the X-ray source and the detector. As the X-ray source and the detector move in the given range of angle and sample is rotated with certain rotations per minute, the diffraction patterns are recorded in terms of a graph of the scattered intensity of scattered X-rays vs. 2θ (the angle between the detector and X-ray source). During scanning of X-rays through the sample, if the Bragg's diffraction condition is satisfied by the geometry of incident radiation, constructive interference occurs, and intense peak can be observed in the pattern.

For this experiment the 2θ range selected was from 11-60 degrees, goniometer rotation per minute was 120. It is possible to do the experiment without rotating the goniometer containing the sample, but this is not a good idea if one wants to get the good intensity peaks. If the samples are rotated with appropriate rotations per minute, the samples inside the capillaries would be positioned at least once in its best orientation to X-rays, so that the sample can diffract X-rays with better intensity.

In order to carry out PXD of these air-sensitive samples, the capillaries having a 0.5 mm diameter were filled inside the glove box. Capillaries for references that were not air-sensitive were prepared outside the glove box. If the capillaries prepared for PXD is not fully compact or if the capillary is not properly mounted and not aligned properly in the goniometer, then the sample may not be oriented properly with respect to the X-rays and then it is possible not to obtain good quality data and hence the graph.

4. Data processing and analysis

4.1. TGA-DCS data analysis

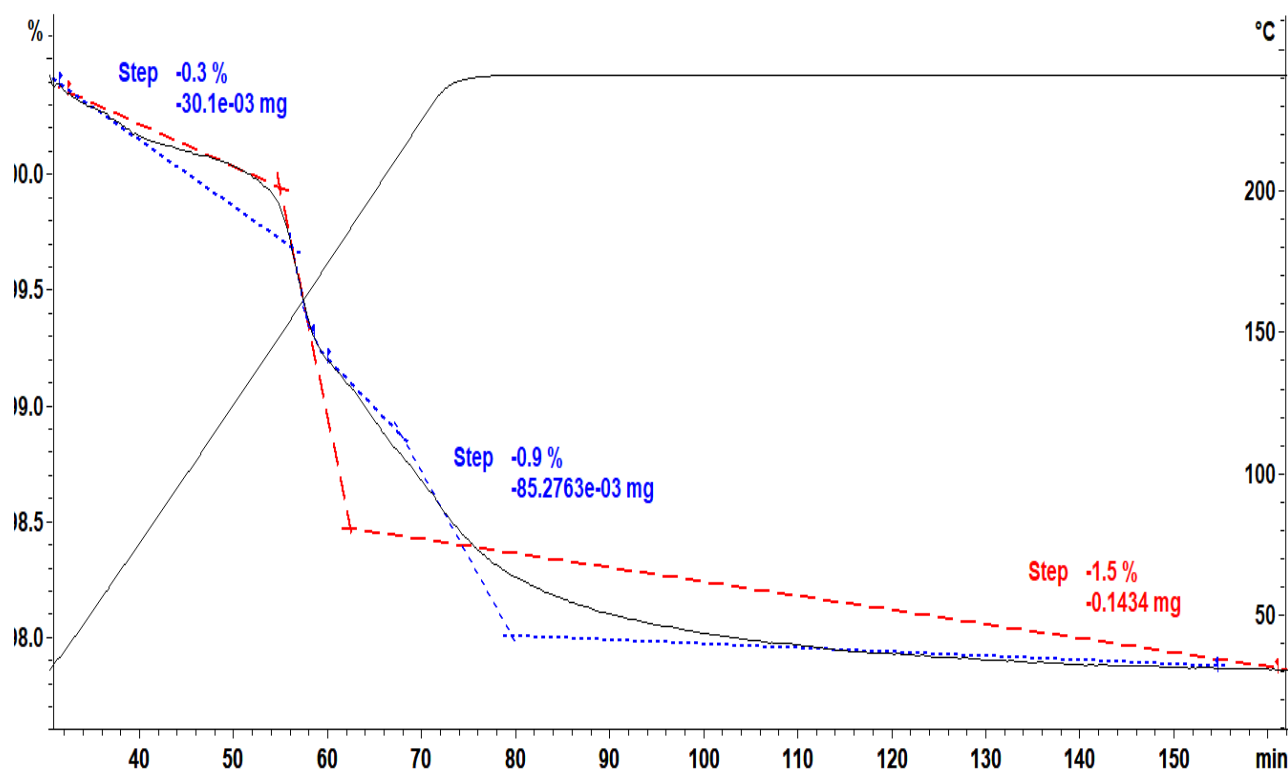
Hydrogen gravimetric desorption measurements were performed using the combined differential scanning calorimetry-thermogravimetric analysis (DSC-TGA) instrument from METTLER TOLEDO. The samples were heated at different decomposition temperatures and the heating rate of 5K/min in a 200 ml/min Ar flow. The samples were heated to a required temperature at 5 K/min and then left to decompose at isothermal conditions.

| S.N | Decomposition temperature (°C) | Reaction isotherms | Initial Mass of sample (mg) | Weight loss (mg) | % weight loss Per sample |
|-----|--------------------------------|--------------------|-----------------------------|------------------|--------------------------|
| 1. | 240 | 19 hrs | 9.8 | 0.1434 | 1.5 |
| 2. | 260 | 16 hrs | 10.9 | 0.2 | 2.1 |
| 3. | 280 | 16 hrs | 9.7 | 0.3602 | 3.7 |
| 4. | 300 | 3 hrs | 10.8 | 0.6246 | 5.8 |
| 5. | 320 | 3 hrs | 11.2 | 1.0479 | 9.4 |
| 6. | 340 | 4 hrs | 10.4 | 1.1145 | 10.7 |
| 7. | 400 | 2 hrs | 11.96 | 0.962 | 11.3 |

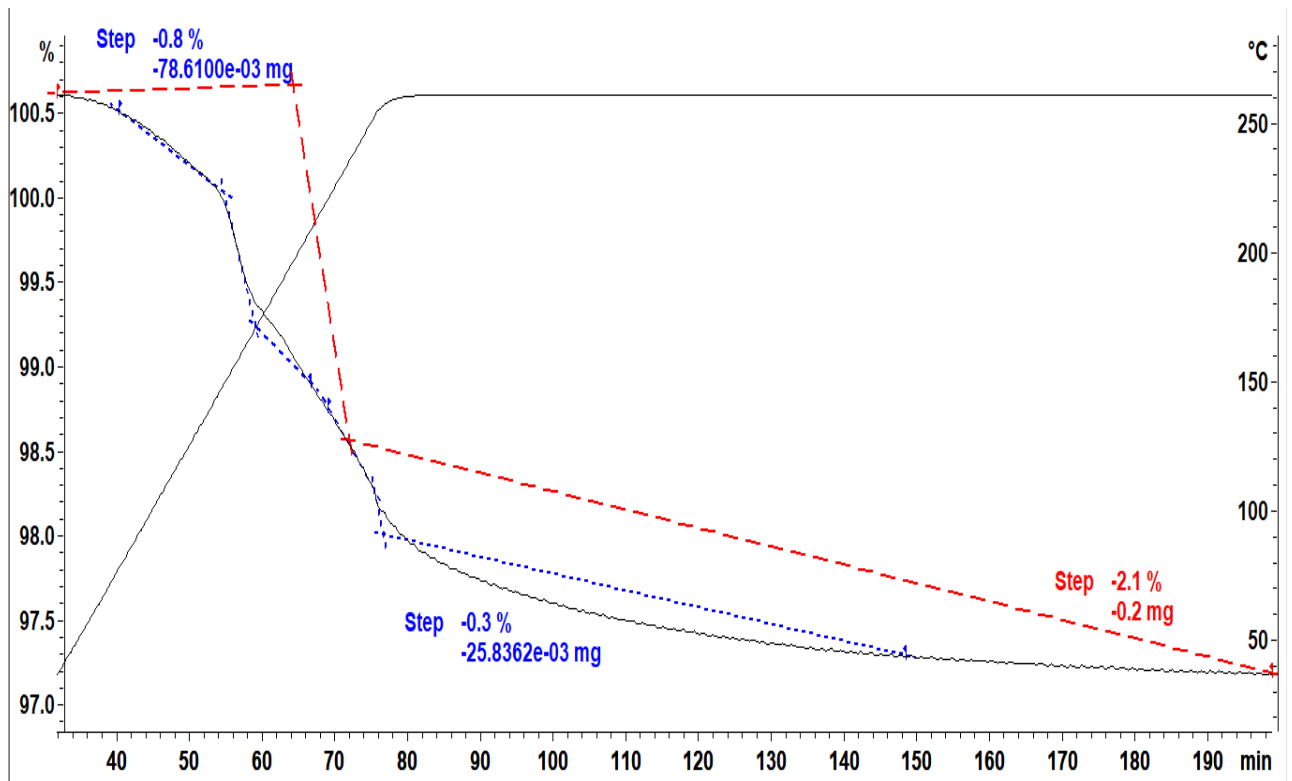
Table 4.1: TGA-DSC details of the samples prepared at different temperatures

Graphs given below show the details of total weight loss in the samples decomposed at different temperatures and at different reaction times. It also shows the total weight loss in the sample in terms of its weight in 'mg' and the percentage.

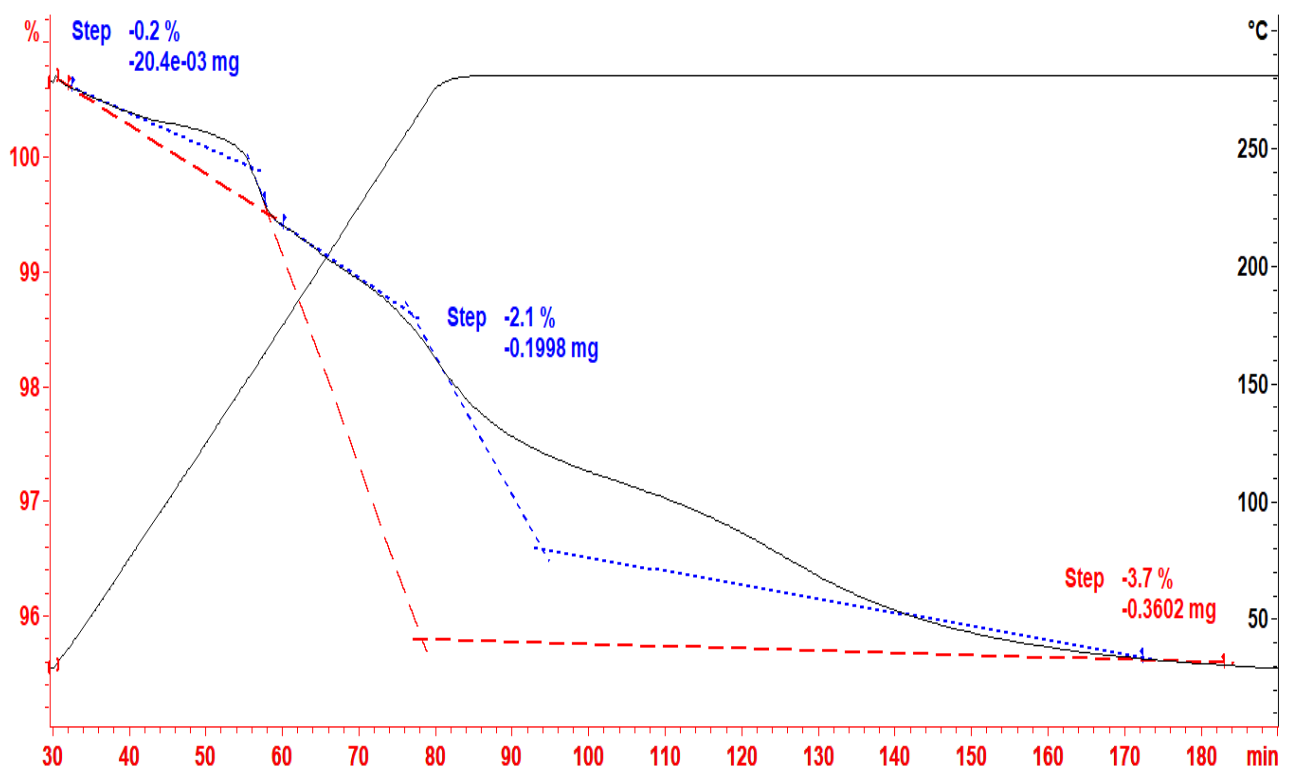
a)



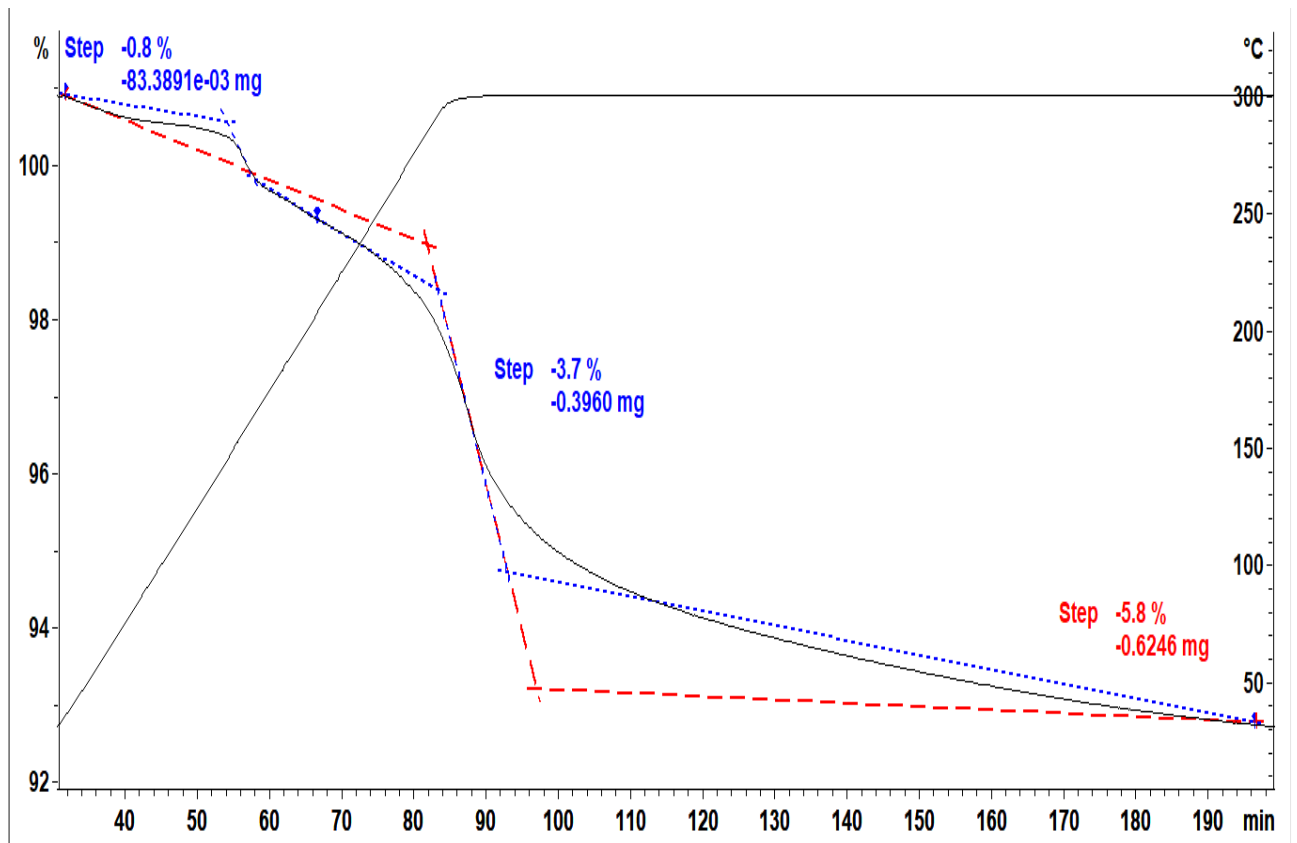
b)



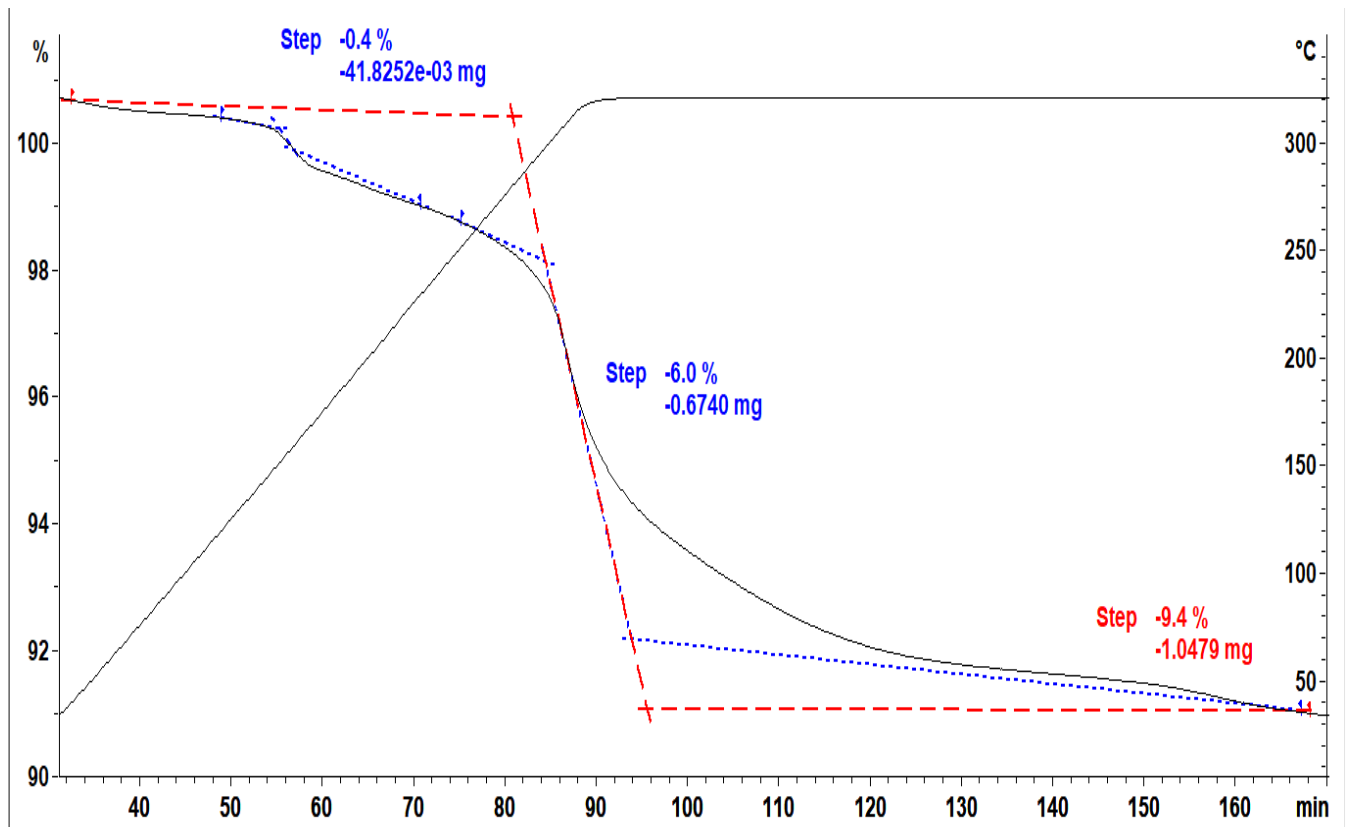
c)



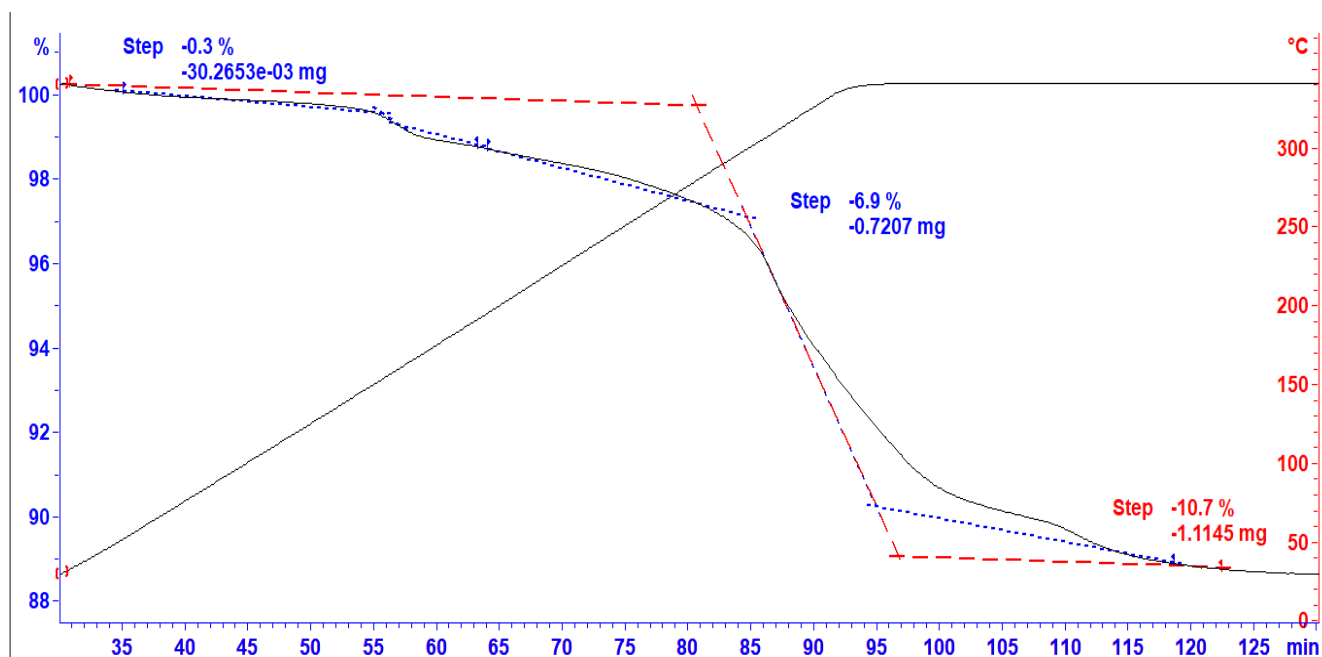
d)



e)



f)



g)

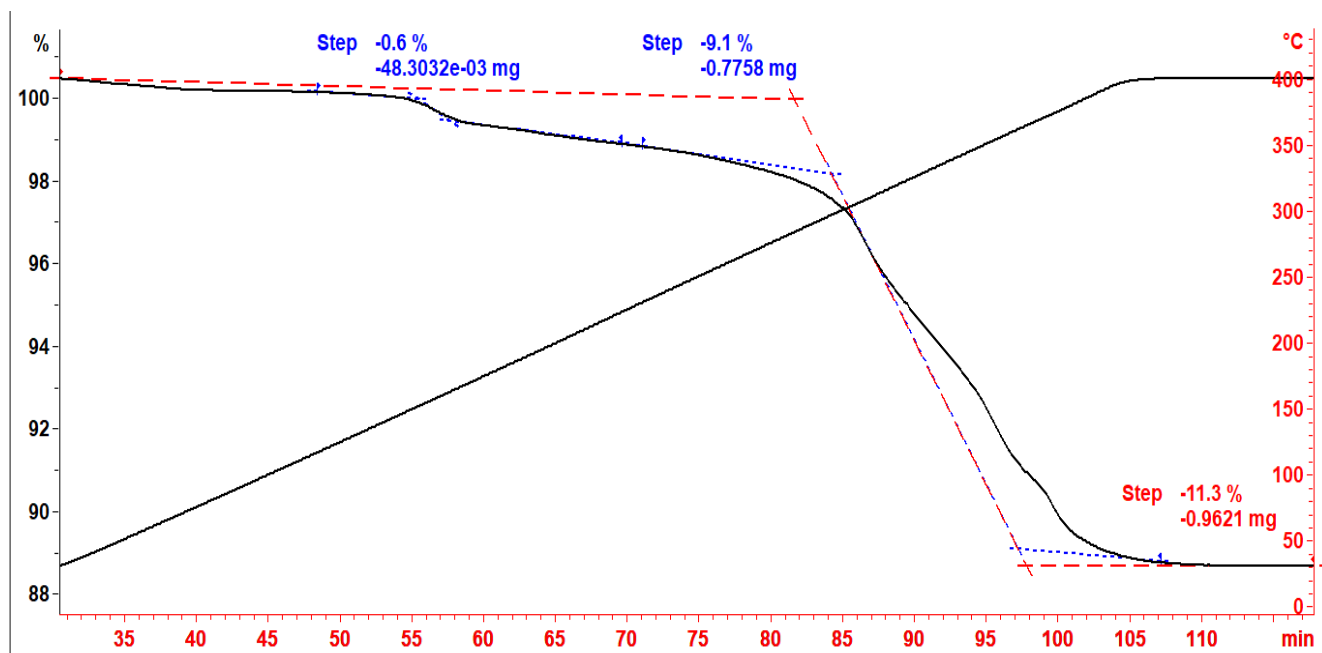


Figure 4.1: Weight loss in the samples during decomposition of γ - $\text{Mg}(\text{BH}_4)_2$ in TGA/DSC instrument in two septs for a) 240°C b) 26°C c) 280°C d) 300°C e) 320°C f) 340°C and g) 400°C. The red dashed line shows the total weight loss during the decomposition of the samples whereas the blue dotted line shows the weight loss in two steps in selected regions. The sample temperature during reaction is denoted by a black straight line while the other black curve is the TGA curve that shows weight loss during the reaction.

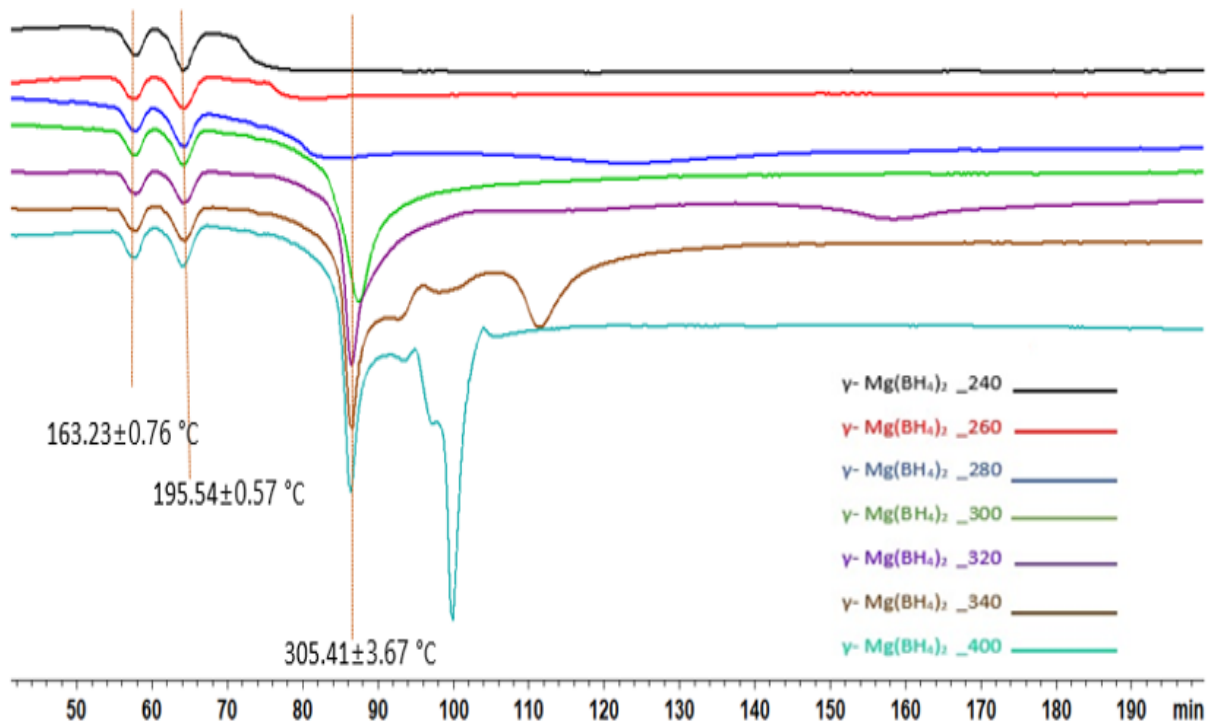


Figure 4.2: DSC curves showing heat flow through the samples with endothermic events at different temperatures. The peak temperatures are indicated as the mean ± STD (2 significant digits) shown in the figure.

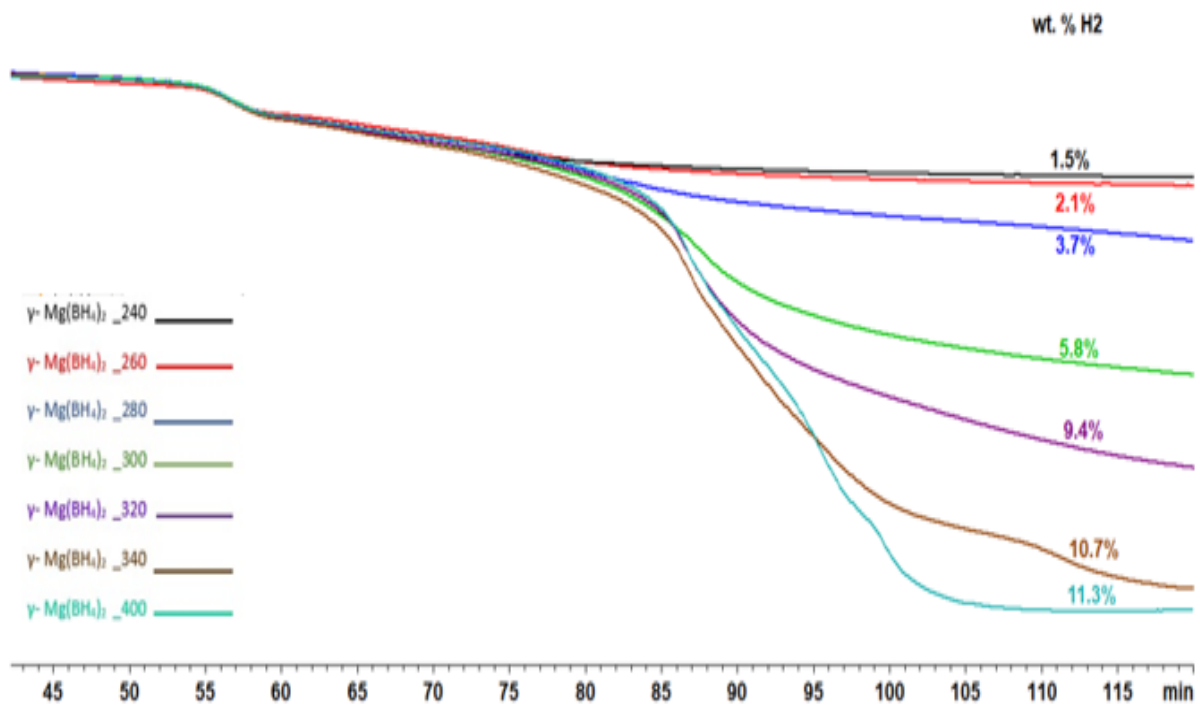


Figure 4.3: TGA curves showing the weight loss of the sample during the decomposition of samples at different temperatures.

The combined DSC and the TGA curves for all the samples decomposed at different temperatures are shown in figures 4.2 and 4.3 above. These curves altogether have shown the progress of the reaction on during step by step heating from 240°C to 400°C by providing supporting information for each other. For γ -Mg(BH₄)₂ the weight loss has been observed from very low temperatures below 100°C, but has no evidence of released reaction product at this temperature. Literature has mentioned that it could be associated with the desorption of impurities from the pores of highly porous γ - Mg(BH₄)₂ and/or the sublimation of the sample during heating as stated in [4] and the studies on mass spectroscopy has shown that it can be possible for hydrogen desorption below 100°C.

The first heat flow curve at 240°C comprised with only two endothermic events in the temperature range between 145-215 °C due to the phase transitions of Mg(BH₄)₂ at high temperature from phase γ → unknown phase → β with the weight loss during phase transitions which were observed from the corresponding TGA curves. This result is under the described earlier findings by [4, 7, 15] and agreeing that the decomposition of γ - Mg(BH₄)₂ starts from β as described in section 1.3.2 of this thesis. By combining the information extracted from both TGA and DSC curves at 240°C showed that the third endothermic peak has started growing already with the total weight loss of 1.5 wt% of H₂ meaning that the decomposition has already progressed to form the unknown B-H species. The DSC curve for the samples decomposed at 260 °C and 280 °C showed the growth of the third endothermic peak indicating the progress of decomposition reaction which corresponds to the weight loss in the TGA curves at 260 and 280 °C that showed an increased amount of weight loss in each temperature step. Total weight loss in 260°C was observed to be 2.1 wt % of H₂ whereas in 280 °C it was 3.7 wt % of H₂. Thus, the decomposition progress in each temperature step can be observed with the production of an increased amount of hydrogen gas. In comparison with [4], this weight loss does not agree with the weight loss values and is reported to be 5.9% and 6.8% for the temperatures around 262.5°C and 284.8°C.

The DSC curve for the sample decomposed at 300 °C showed three complete endothermic peaks with its TGA curve showing weight loss of 5.8 wt % of H₂ supporting the continuous desorption of H₂ and formation of B-H amorphous species along with the of formation of new compound around 300°C. From this temperature onwards the weight loss values seem to be increasing significantly. Hence, it can be suggested that, from this temperature, the next step of reaction might have started with a new reaction product along with the B-H species. [15] reported 4.7 wt% of H₂ when the same sample is heated at 295°C.

In the next decomposition stage, DCS curve showed a same but more intense endothermic peak at around 305°C but in additionally, shows one extra broad but growing endothermic peak during its isothermal heating at 320°C for 3hrs by showing a good amount of weight loss of about 9.4% of H₂ as given by TGA curve. The weight loss and the endothermic peaks at this temperature could be referred to as the formation of MgBH₄ and MgB₄ with other B-H species when heated at 320°C in vacuum or H₂ back pressure whereas the weight loss is only 6.1 wt% of H₂ as shown by [15].

At temperatures 340°C and 400°C, the samples showed at least five endothermic peaks which are attributed to the formation of B-H species along with the possibility of various products like MgH₂, MgB₁₂H₁₂ and H₂ at 354°C and only Mg and H₂ when heated at 410°C releasing 1.3 and 3.7 wt % of H₂ respectively [15]. But the weight loss values in this work are much better at these temperatures and are given by 10.7 and 11.3 wt% of H₂ for 340°C and 400°C respectively.

All the decomposition products were pale yellow to strong yellow, then brown, and finally gray in color with the stronger tint of samples decomposed at higher temperatures in Ar as reported in [46]. The picture given below shows the beautiful color variations in the samples prepared at different

temperatures starting from fresh γ - $\text{Mg}(\text{BH}_4)_2$ and then the heated γ - $\text{Mg}(\text{BH}_4)_2$ from temperature 240°C to 400°C.

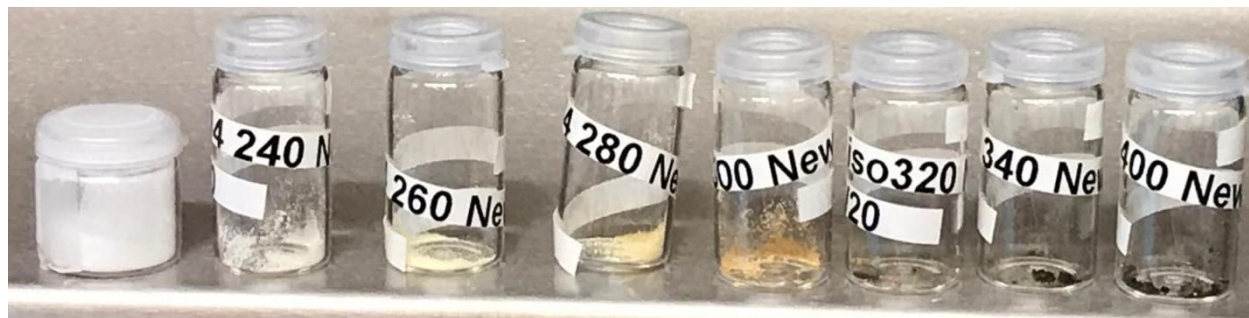


Figure 4.4: Color variation from fresh to the decomposed γ - $\text{Mg}(\text{BH}_4)_2$ from 240°C to 400°C using TGA/DSC 3+.

The table below shows the calculated hydrogen molecule release from each reaction conducted in different temperatures provided the Ar atmosphere and 5K/min heating rate in the TGA-DSC instrument. The last column predicts the remains of the reaction in every temperature step based on the amount of hydrogen released.

In the following way, the last column values can be achieved.

The total molecular weight of one $\text{Mg}(\text{BH}_4)_2$ molecule = 53.99 a.m.u

Let us take the hydrogen release by wt % in 240 °C = 1.5 %

So, the total weight loss of H = 1.5 % of 53.99 = 0.81 a.m.u = 0.81 H atoms

In terms of H-molecule of 0.81 H atoms = 0.4 H_2

Thus, the remaining number of H in the reaction product left = $8 - 0.4 \times 2 = 7.2$ and hence the predicted remain of the reaction, in this case, = $\text{MgB}_2\text{H}_{7.2}$

By using this concept, the possible number of H- atom left in the product can be calculated as;

| γ - $\text{Mg}(\text{BH}_4)_2$ decomposition temperature (°C) | % weight loss Of H_2 | Calculated no. of released H_2 (hydrogen molecule) | Possible product of the reaction |
|--|-------------------------------|---|----------------------------------|
| 240 | 1.5 | 0.4 | $\text{MgB}_2\text{H}_{7.2}$ |
| 260 | 2.1 | 0.6 | $\text{MgB}_2\text{H}_{6.8}$ |
| 280 | 3.7 | 1 | MgB_2H_6 |
| 300 | 5.8 | 1.6 | $\text{MgB}_2\text{H}_{4.8}$ |
| 320 | 9.4 | 2.5 | MgB_2H_3 |
| 340 | 10.7 | 2.9 | $\text{MgB}_2\text{H}_{2.2}$ |
| 400 | 11.3 | 3.1 | $\text{MgB}_2\text{H}_{1.8}$ |

Table 4.2: Calculated numbers of released hydrogen molecules and the remaining reaction product in each temperature step assuming that the weight loss is only because of hydrogen.

4.2 XRD data analysis

Powder X-ray diffraction (PXD) of the samples and references were carried out in the D8 Advance Diffractometer situated in UiS Materials' Science laboratory. The diffraction patterns were obtained in a Debye-Scherrer geometry using Cu-K α radiation of wavelength (λ) 1.5418 Å. All the diffraction data were collected at room temperature whereas the samples were prepared inside the glove box. The sample for PXD was prepared in the glass capillaries with an external diameter of 0.5 mm. Data analysis was done by using DIFFRACT.SUITE together with OriginPro 2020b. Background subtraction was done by DIFFRACT.SUITE software whereas the data plotting was done completely in the OriginPro 2020b.

The samples were tried to fill up to 2 cm height from the bottom of the capillary which is the standard amount of the sample to be filled for the XRD. In some cases, the amount of sample obtained after TGA-DSC operation was very little and hence it was not possible to fill up the capillary up to the standard 2 cm height. Sometimes the amount of sample obtained was grains that got stuck between the capillary, not allowing the samples passing through it up to the bottom and not allowing samples to be filled with full compactness. Particularly, the amount inside the capillaries for references was almost up to 2 cm height or even more, but for the samples decomposed in temperatures, 400, 340 and 300°C were not enough to be filled up to the standard height and was about 1 cm height inside the capillaries. Sample decomposed at 320 and 280°C were filled up to almost 2 cm. The best-prepared capillaries were for the samples decomposed at 240 and 260°C. These samples were filled as soon as they were prepared in the TGA/DSC instrument so had less chance for oxidizing and during the preparation of capillaries, they were pressed well with poker so that the samples were compact enough to produce good quality data. The other samples were filled inside the capillaries at least one week after their preparation.

Prediction of the peak positions

Theoretical peak positions of samples and references were obtained by combining the idea of Bragg's diffraction with the formula of interplanar spacing in the crystals. Following table shows the (hkl) peak positions in XRD pattern of the references and samples for the angle of diffraction 2θ such that;

$$0 < 2\theta < 60.$$

| Name of the compound | Crystal system | Space group | Allowed hkl | 2 θ (degrees) |
|--|----------------|---------------------------|--------------------------------|----------------------|
| MgB ₂ | Hexagonal | <i>P6/mmm</i> | 0001 | 25.2 |
| | | | 10-10 | 33.7 |
| | | | 10-11 | 42.5 |
| | | | 0002 | 51.7 |
| | | | 2-1-10 | 60.2 |
| α -MgH ₂ | Tetragonal | <i>P4₂/mnm</i> | 110 | 27.9 |
| | | | 101 | 35.8 |
| | | | 200 | 39.9 |
| | | | 211 | 54.7 |
| | | | 220 | 57.8 |
| MgO | Cubic | <i>Fm-3m</i> | 111 | 36.6 |
| | | | 200 | 42.5 |
| Mg | Hexagonal | <i>P6₃/mmc</i> | 10-10 | 32.3 |
| | | | 0002 | 35.0 |
| | | | 10-11 | 36.8 |
| | | | 10-12 | 48.3 |
| | | | 2-1-10 | 57.6 |
| γ - Mg(BH ₄) ₂ (Fresh) | Cubic | <i>Ia-3d</i> | 211 | 13.7 |
| | | | 220 | 15.8 |
| | | | 321 | 20.9 |
| | | | 420 | 25.1 |
| | | | 422 | 27.6 |
| | | | 510 | 28.7 |
| | | | 420 | 31.9 |
| | | | 532 | 34.9 |
| | | | 620 | 35.8 |
| | | | 631 | 38.5 |
| | | | 444 | 39.4 |
| | | | 640 | 41.1 |
| | | | 552 | 41.9 |
| | | | 642 | 42.7 |
| | | | H ₃ BO ₃ | Triclinic |
| 011 | 15.1 | | | |
| 101 | 18.3 | | | |
| 1-10 | 20.7 | | | |
| 10-1 | 21.5 | | | |
| 200 | 26.7 | | | |
| 211 | 27.4 | | | |
| 201 | 28.5 | | | |
| 022 | 30.5 | | | |
| 20-1 | 32.7 | | | |
| | 2-1-1 | 33.9 | | |

Table 4.3: The predicted diffraction peak positions of reference elements and compounds calculated by using the Debye- Scherrer technique and compared from [47].

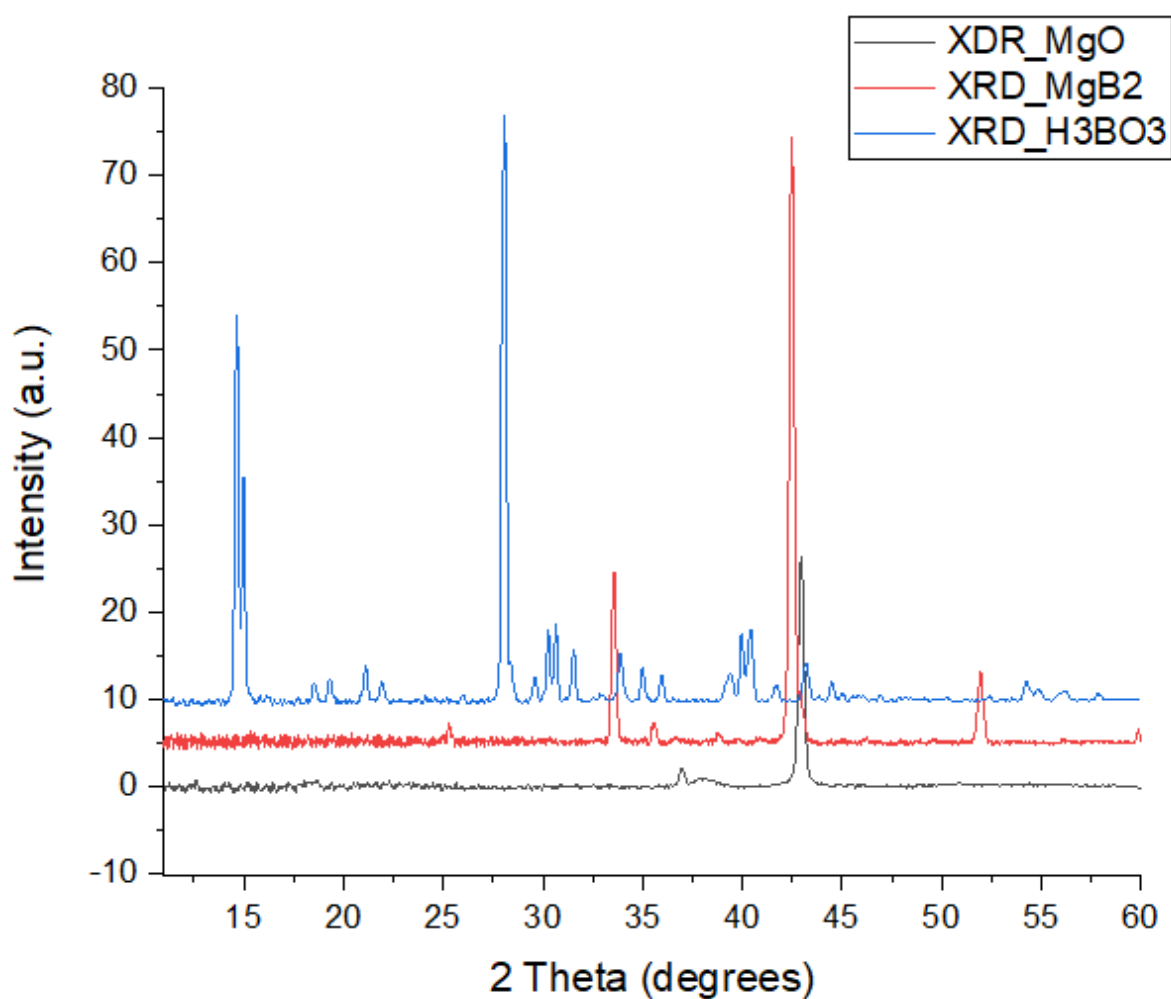


Figure 4.5: Experimental XRD pattern for reference compounds

The figure above shows the experimentally observed XRD patterns for magnesium oxide (MgO) (figure 4.5 (black)), magnesium boride (MgB₂) (figure 4.5 (red)), and the boric acid (H₃BO₃) (figure 4.5 (blue)), which are in complete accordance with the calculated XRD peak positions. The figure below shows the experimentally obtained XRD patterns for the samples decomposed at different temperatures along with the fresh γ -Mg(BH₄)₂ as a reference.

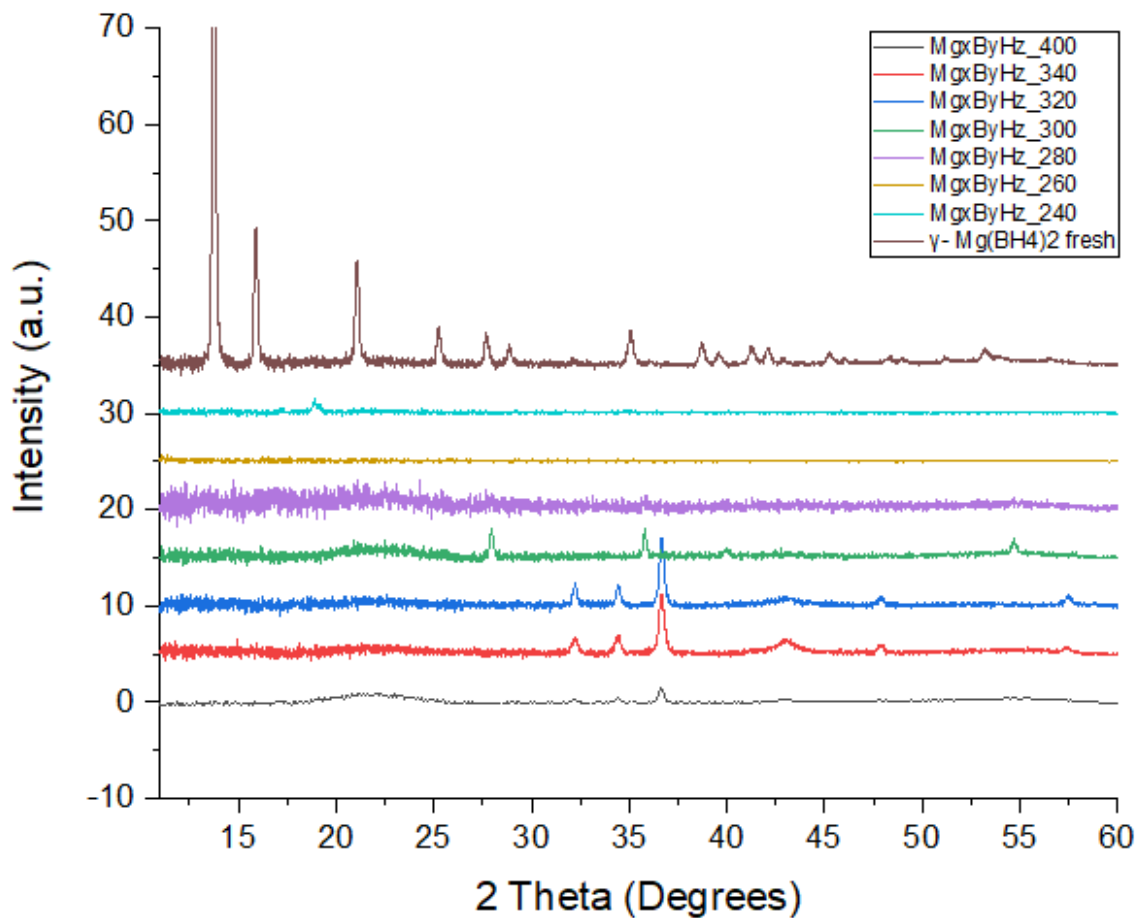


Figure 4.6: Experimental XRD pattern for fresh and dehydrogenated and γ - $\text{Mg}(\text{BH}_4)_2$ at different temperatures obtained from OriginPro 2020b

The background-subtracted XRD patterns of the partially decomposed samples showed very small hump in the region between 15 to 25 degrees of 2θ values and confirmed the presence of amorphous products in the earlier stages of decomposition. But some sharp peaks were also observed in later stages which confirmed the presence of the crystalline compound. The less intense peak at about 18.8 degrees in the XRD pattern of the partially decomposed γ - $\text{Mg}(\text{BH}_4)_2$ at 240°C corresponded with the most intense peak of $(\epsilon+\beta')$ - $\text{Mg}(\text{BH}_4)_2$ agreeing with the XRD result presented in [7].

No trace of PXD peaks was observed for the samples decomposed at 260°C and 280°C confirming the complete decomposition of γ - $\text{Mg}(\text{BH}_4)_2$ after 260°C. The possible amorphous compounds in this temperature range were confirmed to be only amorphous B-H species. For the samples decomposed at 300 °C, five strong peaks were observed which corresponded with the calculated peak positions of the α - MgH_2 in the range between 11 to 60 degrees confirming the presence of α - MgH_2 along with the amorphous B-H species at this temperature.

The partially decomposed samples at 320°C and 340°C, coinciding five sharp peaks with each other in both the spectra, with the most intense peak at an angle of 36.7 degrees and a broad feature at around 42 degrees. All five diffraction peaks completely corresponded with the calculated XRD peaks and hence confirmed the presence of hexagonal magnesium crystal. The broad peak at about 42 degrees

is associated well with the calculated most intense peak for the cubic structure of magnesium oxide (MgO). When obtained the XRD pattern for the sample decomposed at 400°C, showed only three peaks with small intensities in the same position as in 320°C and 340°C samples. These peaks corresponded as with the XRD peak positions of the first three most intense peaks of the hexagonal crystal structure of magnesium (Mg) but reduced in intensities of each peak indicating the formation of some other compounds in the expense of reduced magnesium.

The table below concludes the possible compound formation in the partially decomposed samples at different temperatures as confirmed by the PXD pattern.

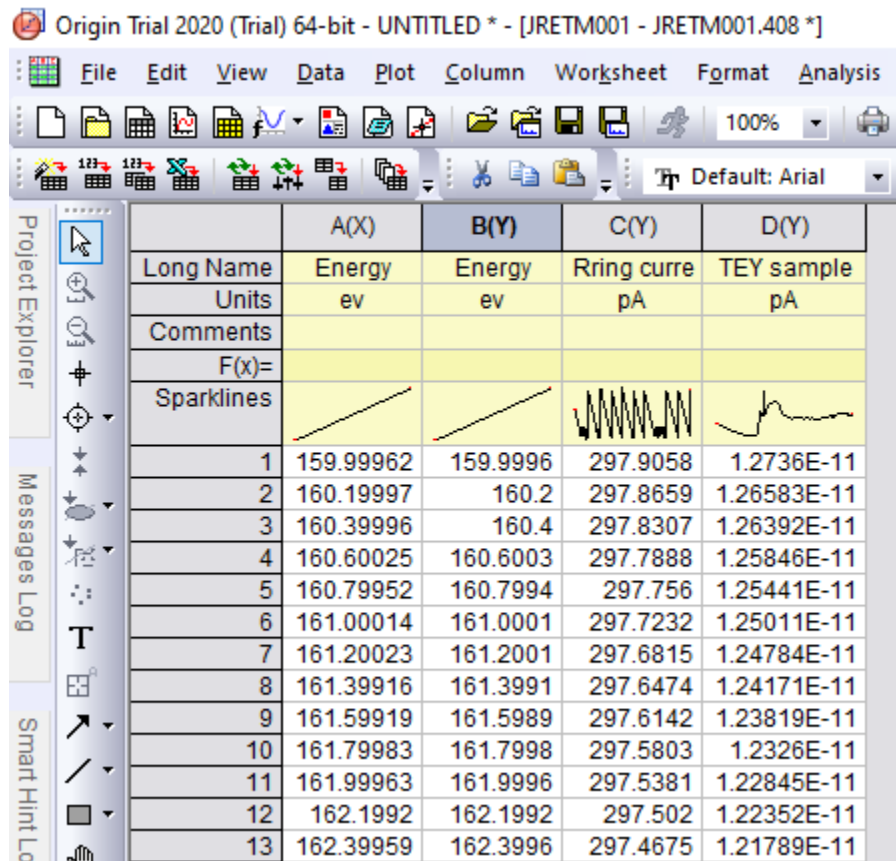
| Temperature of Partially decomposed samples (°C) | Presence of compounds at different temperatures, observed from XRD pattern |
|--|--|
| 240 | A small amount of (β)- Mg(BH ₄) ₂ + amorphous B-H species |
| 260 | Only amorphous species |
| 280 | Only amorphous species |
| 300 | A good amount of α-MgH ₂ + amorphous B-H species |
| 320 | Hexagonal Mg crystal + small amount of MgO + amorphous B-H species |
| 340 | Hexagonal Mg crystal + small amount of MgO + amorphous B-H species |
| 400 | A small amount of Mg crystal + amorphous B-H species |

Table 4.4: Compounds present on the samples decomposed at different temperatures as confirmed by PXD pattern

The XRD data confirmed that when γ- Mg(BH₄)₂ is decomposed at 240°C, along with the formation of B-H amorphous species, there is still some amount of the (ε+β')- Mg(BH₄)₂ present in the sample which was formed during phase transitions of γ - Mg(BH₄)₂ in the temperature range, between 150-215°C, as mentioned earlier in section 1.3.2. So, it is confirmed that the sample is not completely decomposed until 240°C. According to the data obtained in PXD, the sample prepared at 260°C and 280°C is completely decomposed with the formation of only amorphous B-H species which is in good agreement with the reaction products given in the literature mentioned in the section 1.3.2. At the temperature of 300 °C, the data shows the formation of crystalline α-MgH₂ along with the amorphous B-H species but after 300°C, at 320 the MgH₂ is already completely decomposed to magnesium by showing disagreement with the reaction no. 1.14, 1.15, and 1.16 given in the literature [7]. Along with the formation of hexagonal Mg crystals, a small amount of MgO formation has also been observed at 320°C and 340°C, which is supposed to be because of the oxidization of the samples. The sample decomposed at 400 °C shows the small amount of magnesium along with the unknown amorphous species, which is in partial agreement with equation (1.4) of section 1.3.2 which shows the decomposition of MgH₂ to Mg and H₂ between the temperature range (365°C-410°C) but not completely agreeing with the result of the formation of Mg from the temperature 340 °C as in reaction equation (1.5) of section 1.3.2, instead of 320 °C in this PXD studies.

4.3. XANES data Analysis

The measured data was available in .txt format including all the relevant parameters and measured values. For data processing, extraction, and formatting of the only parameters of interest were done by using OriginPro 2020b. From the experiment, we obtained the total electron yield values in terms of drain current (pA), with the corresponding energy values and the ring current for each data. The energy range used for the measurement at boron K-edge was 160-260 eV. The table below shows the data format that was obtained from the beamline.



| | A(X) | B(Y) | C(Y) | D(Y) |
|------------|-----------|----------|------------|-------------|
| Long Name | Energy | Energy | Ring curre | TEY sample |
| Units | ev | ev | pA | pA |
| Comments | | | | |
| F(x)= | | | | |
| Sparklines | | | | |
| 1 | 159.99962 | 159.9996 | 297.9058 | 1.2736E-11 |
| 2 | 160.19997 | 160.2 | 297.8659 | 1.26583E-11 |
| 3 | 160.39996 | 160.4 | 297.8307 | 1.26392E-11 |
| 4 | 160.60025 | 160.6003 | 297.7888 | 1.25846E-11 |
| 5 | 160.79952 | 160.7994 | 297.756 | 1.25441E-11 |
| 6 | 161.00014 | 161.0001 | 297.7232 | 1.25011E-11 |
| 7 | 161.20023 | 161.2001 | 297.6815 | 1.24784E-11 |
| 8 | 161.39916 | 161.3991 | 297.6474 | 1.24171E-11 |
| 9 | 161.59919 | 161.5989 | 297.6142 | 1.23819E-11 |
| 10 | 161.79983 | 161.7998 | 297.5803 | 1.2326E-11 |
| 11 | 161.99963 | 161.9996 | 297.5381 | 1.22845E-11 |
| 12 | 162.1992 | 162.1992 | 297.502 | 1.22352E-11 |
| 13 | 162.39959 | 162.3996 | 297.4675 | 1.21789E-11 |

Figure 4.7: Data format obtained from the beamline imported in Origin 2020b.

4.3.1. Data treatment were done in the following steps:

1. Extraction of the required file where the file contains information as shown in the table above.
2. Incident X-ray flux, I_0 was measured concurrently as the drain current to a gold-coated mesh located along the X-ray beam path and upstream of the experimental sample.

For calculation of I_0 , the following steps were followed;

- a) The measured TEY for B K-edge from the Au foil was normalized to the ring current by dividing the TEY signal by ring current value.
- b) The flux was obtained by dividing the normalized TEY signal (a) by the absorption-cross section of gold:

$$flux(I_0) = \frac{TEY (Au)}{\{ring\ current\} \cdot \sigma_a^{Au}}$$

3. Once the I_0 was obtained, the TEY signals for the sample was be normalized to the ring current and then the normalized TEY signal was divided by the flux (I_0), obtained in 2 (b) to find out the absorption cross-section of the sample:

$$I/\sigma_a^{sample} = \frac{TEY (sample)}{\{ring\ current\} \cdot flux(I_0)}$$

4. Next, the absorption cross-section value for each sample was modified by subtracting the user-defined background by taking some points from the pre-edge and the post- edge region. The Intensity value then obtained after background subtraction was normalized between [0,1].
5. At this stage, the normalized intensity for each sample was ready to compare and move forward for qualitative analysis.

4.3.2. Qualitative data analysis of boron K-edge XANES spectra:

The spectral features of any compound are the result of their molecular structure. The type and the strength of the bond formed between the atoms making the molecule are ultimately determined by the atomic structure of the atom forming it. This is the reason for having different charge distribution in different molecules even though they are formed by the same atoms but different in number or different atoms. The difference in charge distribution results in the different chemical environment around X-ray absorbing atom in XANES. This results in distinct XANES spectra of molecules/compounds with the absorption edge shifts in the XANES regime. In this case, the co-ordination and the chemical environment around B in the compounds like H_3BO_3 , B_2O_3 , $Mg(BH_4)_2$, or MgB_2 determine the XANES spectra and the different position of edge energy of boron. Literature provided in section 2.4.6 explains that the pre-edge region is strongly affected by the bound state of the atom absorbing X-rays. In the present scenario, the X-ray absorption site is always the B atom. As the oxidation state of boron increases, the absorption edge energy increases correspondingly. This can be explained based on the fact that the atom with a higher oxidation state requires a more energetic X-ray to excite its core electron because the nucleus is less shielded and carries a higher effective charge [37] .

Hence, the knowledge on the oxidation state, coordination number, and the electronic transitions are very important to interpret the XANES spectra qualitatively. Once one has the library of references with the structure of the XANES spectra, the spectra of unknown species can be analyzed by the comparison XANES spectra to the known references.

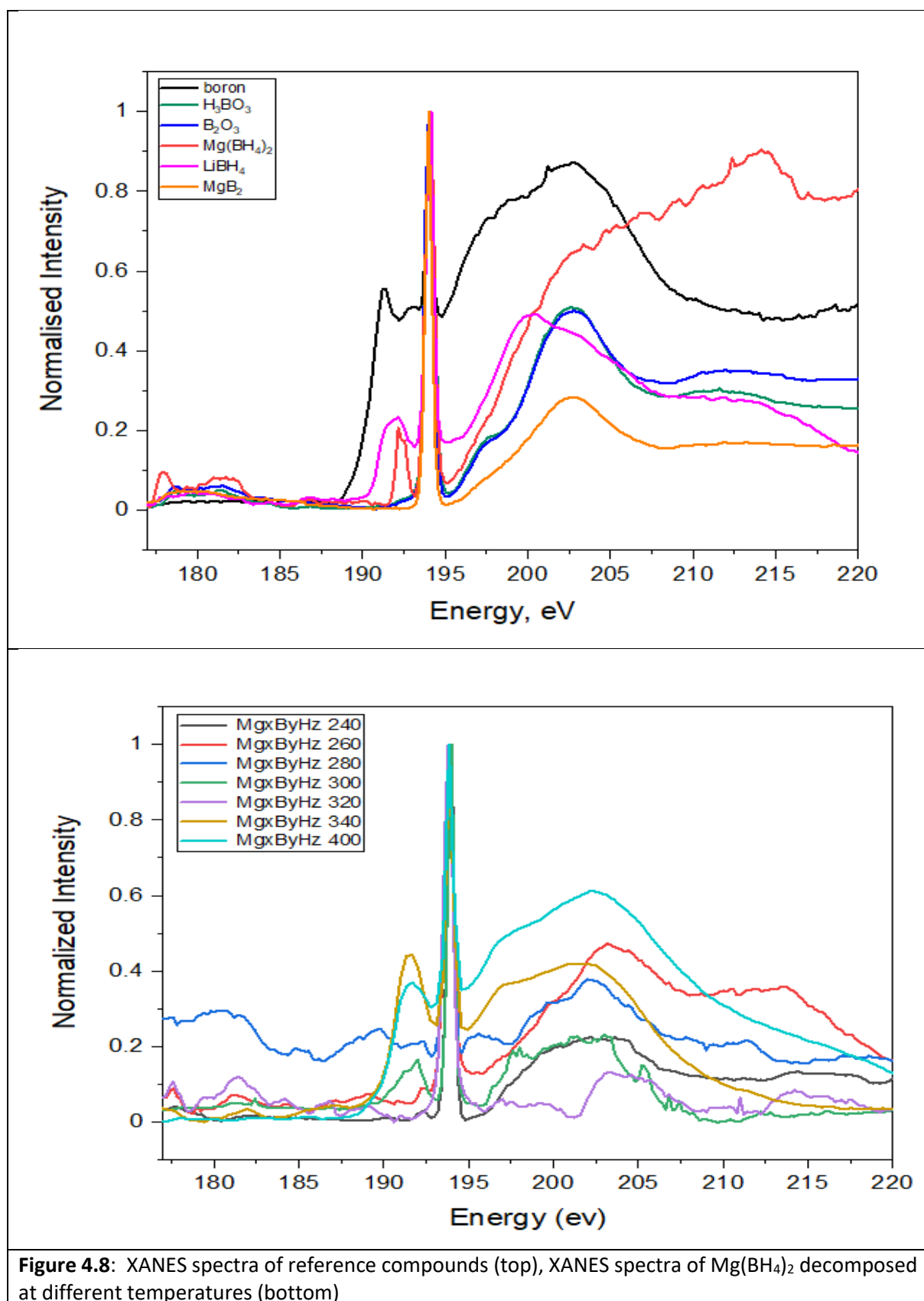


Figure 4.8: XANES spectra of reference compounds (top), XANES spectra of Mg(BH₄)₂ decomposed at different temperatures (bottom)

The spectra of borates (H_3BO_3 and B_2O_3) (Figure 4.8, (top), green and blue spectra) were analyzed in order to observe the coordination of boron in those compounds, which are important compounds that can be possibly observed in the spectrum of the partially dehydrogenated $\gamma\text{-Mg}(\text{BH}_4)_2$. The XANES spectra for H_3BO_3 and B_2O_3 revealed the presence of trigonal $(\text{BO}_3)^{-3}$ and tetrahedral $(\text{BO}_4)^{-5}$ clusters of B characterized by the sharp peak at around 194 eV showing the presence of trigonal B and the diffuse band between 195-208 eV showing the presence of tetrahedral B. The sharp peak at around 194 eV is due to the transition of B 1s electrons to the unoccupied B $2p_z$ orbital which lies below the 1s ionization potential. The peak at 197.6 eV for both of these compounds is assigned to the transition of B 1s electrons to the unoccupied B-O sigma antibonding (σ^*) orbital. Another diffuse band at around 196.8-207 eV with the intense peak at 203 eV, is probably due to the contribution from multiple scattering resonance as reported by [48].

In $\gamma\text{-Mg}(\text{BH}_4)_2$ (Figure 4.8, (top), red spectrum) two tetrahedral BH_4 groups are coordinated by Mg atoms from the two opposite sides and four hydrogen atoms around the B indicating the tetrahedral coordination of Boron [49]. The XANES spectra for $\text{Mg}(\text{BH}_4)_2$ collected in this experiment showed one sharp peak at about 192 eV and another sharp peak at 194 eV supporting the study by Jeong et al. [50] on XAS spectra of freshly prepared $\gamma\text{-Mg}(\text{BH}_4)_2$. The sharp peak at 194 eV probably representing the formation of B_2O_3 on the surface of the sample but there is one important feature at around 192 eV was suggested to be because of the presence tetrahedral co-ordination of B with four H atoms in BH_4^- ion.

In B K-edge XANES spectra of lithium borohydride (LiBH_4) (Figure 4.8, (top), purple curve), the first peak was observed at 192.1 eV, lies between 191.1-193.1 eV. Along with the contribution of oxides which has the most intense peak at 194 eV, another peak was observed at 200 eV which is present in between the broad diffusion band between 195- 208 eV. This peak lies in the same region as in other references, except $\text{Mg}(\text{BH}_4)_2$ but the peak is shifted from 203 eV to 200 eV. The peak at 192.1 eV and 200 eV in the diffusion region indicated the contribution of tetrahedral boron in $(\text{BH}_4)^-$ but the broadness around 192.1 eV peak and the shifted peak of tetrahedral B, from 203 eV to 200 eV is suggested to be because of the presence of small presence of $\text{Li}_2\text{B}_{12}\text{H}_{12}$ in LiBH_4 studied from NMR experiment reported in [51, 52]

Theoretically, magnesium boride (MgB_2) should have a leading-edge at 186.8 eV as a result of $2p_{xy}$ final states above the fermi level according to [42], but in the present work, no such peak at the mentioned energy was observed (Figure 4.8, (top) orange curve). In the experimental TEY results presented by [42] for oxidized MgB_2 corresponded with the result of MgB_2 in the present scenario by not showing the leading edge at 186.8 eV. So, it can be argued that probably the MgB_2 used for this work was oxidized. MgB_2 showed trigonal boron coordination as in B_2O_3 at around 194 eV which is originated from planar three-fold coordinated boron atoms in both compounds. In B_2O_3 , boron is surrounded by three oxygen atoms whereas in MgB_2 , boron is surrounded by other three boron atoms which are in accordance with earlier studies by [48] and [42].

The XANES spectra of boron showed a unique structure and peaks at different positions than other references (Figure 4.8, (top) black curve). One sharp peak was observed in 191.2 eV. This is assigned to the tetragonally coordinated boron, e.g., the transition of B 1s electrons to the unoccupied B 2p states. The strong peak at 194 eV peak in this case as well should probably have contributed from boron oxide formation. The big broad diffusion band from 195- 208 eV was observed with a small peak at 197.59 eV aroused from 195 eV and continued to another broad but intense peak at 203 eV which finally concluded at 205 eV. The XANES B K- edge spectra of $\beta\text{-B}_{105}$ showed similar structure which was suggested to be because of icosahedral geometry where each boron is six-fold coordinated with five boron atoms in its own B_{12} icosahedron and one B atom in a neighboring icosahedron [53]. Besides this, all the B K-edge XANES spectra showed similar features in the energy range between 178-183 eV

but no evidence associated with this has been found to suggest the local environment around the given energy range.

Figure 4.8 (bottom), shows the experimentally obtained Synchrotron XANES B K-edge spectra for partially decomposed γ -Mg(BH₄)₂. A qualitative comparison was made between these spectra with the reference spectra measured at the same experimental conditions. The strongest feature in all the spectra of the samples in (Figure 4.7 (bottom)) was observed at 194 eV which is associated with the formation of B₂O₃ on the surface of the highly air-sensitive samples. This feature evidences that the samples were highly oxidized already before the XANES measurements.

In Figure 4.8 (bottom), starting from the minimum energy, one small peak at 177.59 eV is overlapped for samples at 260 and 320°C showing some common feature. From the range between 178- 183 eV, all the samples show similar features with more or less intensity except in the samples decomposed at 240 and 400°C. The peak at 194 eV and the 195-208 eV region is suggested to be the contribution from the B₂O₃ structures characterized trigonal B at 194 eV and tetragonal boron in the region from 195- 208 eV as compared the XANES spectra of samples with the spectra of B₂O₃.

The spectra of the samples decomposed at 240°C and 260°C showed almost the same features. Both showed the peak at 192 eV for tetrahedral coordination of boron possibly BH₄⁻ ion as obtained from the spectra of fresh γ -Mg(BH₄)₂ and also as suggested in the literature[42] in case of borohydride spectra, but the peak for sample decomposed at 260°C seemed to be less intense, indicating the smaller contribution of tetrahedral boron than in 240°C and showed very little but interesting feature at the post-edge region of the spectra.

The spectra for the sample decomposed at 280°C showed a broad peak at 189.8 eV but a very small peak at around 192 eV indicating the reduced contribution from tetrahedral boron. As soon as the sharp peak of 194 eV ends, other features at 194-197 eV and 197-208 eV regions can be seen. The feature from 197-208 eV showed similar structure as in Boron spectra but the feature from 194-197 eV is not seen in any other spectrum signifying new reaction product at this temperature.

Among all the spectrum, spectrum presented for the decomposed sample at 300°C, seemed to be quite noisy but also has some extra features than in other spectra. The spectrum showed an intense but broad peak at 192 eV. This peak was arising from 187-193 eV indicating the presence of some new B-H group along with the tetrahedral coordination of B. Along with the peak at 198.7 eV and 203 eV, additions features at 205, 206 and 207 eV was also observed. One feature at 212 eV corresponded with the strong feature of fresh Mg(BH₄)₂.

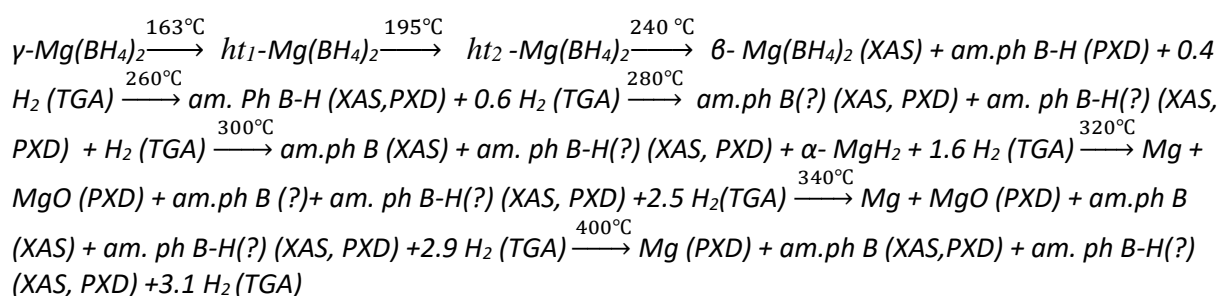
At the next step, for the sample decomposed at 320°C, no peak was observed around 192 eV indicating the absence of tetrahedral coordination of boron. Also, the diffused band is shifted from 201-210 eV but by keeping the peak position at 203 eV which indicates still the presence of trigonal B coordination.

For the samples decomposed at 340°C and 400°C, spectra showed almost the same characteristics indicating almost similar local structure, except the broad feature of 340°C, in the range 178-183 eV. Both showed different pre-edge structures than other spectra and contained the broader feature between 187-193 eV, with a peak position at 191.6 eV. The post-edge feature of both spectra seemed to be almost the same and corresponds to the post edge structure of B spectra.

In conclusion, using the combined experimental approach, we have demonstrated the different reaction phases in the partial decomposition of γ -Mg(BH₄)₂. Experiments showed that the maximum of 11.3 wt% of H₂ desorption at 400°C in the Ar atmosphere, with the production of amorphous B-H species consistently present in all the reaction temperatures. TGA- DSC showed the phase transition

from γ to some unknown intermediate phase which finally decomposed to β - $\text{Mg}(\text{BH}_4)_2$ before the decomposition started. Experiments showed that the weight loss started from the beginning, below 100°C is assigned to the weight loss either due to impurities (H_2O or O_2 molecules) present on the surface of highly porous γ - $\text{Mg}(\text{BH}_4)_2$ or because of the H_2 desorption. Studies from mass spectroscopy have shown that the desorption below 100°C is possible. PXD Confirmed the absence of crystalline compounds in the partially decomposed samples at 260 - 280°C temperatures. But the presence of crystalline compounds at different temperatures clearly indicated the new reaction products at different phases. Combining the results from TGA-DSC, XANES spectrum of B K-edge, and the PXD report, the sample when decomposed from 240 - 300°C comprises the tetrahedral coordination of B probably in terms of BH_4^- ion but there no any evidence was found for tetrahedral boron for the sample decomposed at 320°C . Qualitative comparison of the B K-edge XANES spectrum of the samples decomposed at 340 - 400°C resulted in the conclusion that the broadened feature at around 190 eV indicated the contribution from the combined effect of tetrahedral B along with various B-H species that can include MgB_2 , $\text{MgB}_{10}\text{H}_{10}$ and $\text{Mg}_3(\text{B}_3\text{H}_6)_2$ as reported in [50] when the XANES B K-edge spectra were subtracted with B_2O_3 from the original spectra of the samples.

Our combined experimental approach has shown that the decomposition reaction in γ - $\text{Mg}(\text{BH}_4)_2$ can be summarized as follows:



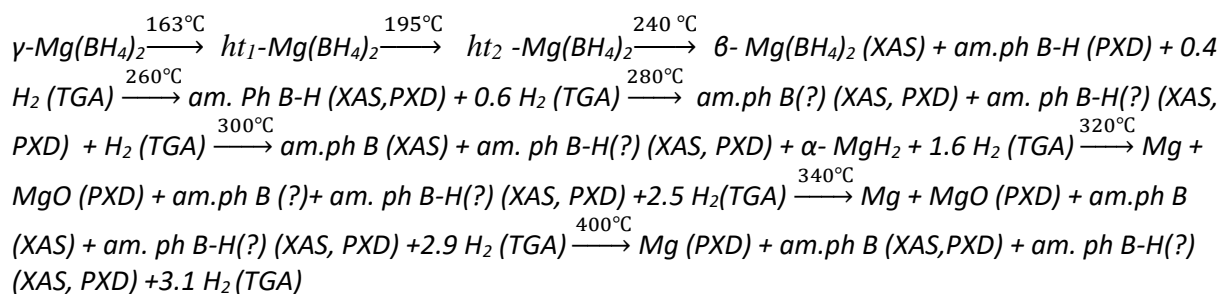
Handling of air-sensitive samples was a challenging but crucial part of the experiments as the experimental results depend on how much is the sample oxidized and how pure is the sample that has been taken for experiments. The experiment on TGA-DSC provided the information about the sample through heat flowing in and out of the sample during the experiment and the weight loss during each endo or exothermic event. PXD proved itself as the best technique by identifying the presence of crystalline reaction product in the sample decomposed at various temperatures. XANES provided information about amorphous boron and the local environment around it. Hence, it is one of the best techniques to study amorphous species through qualitative analysis. The weight loss below 100°C for these samples has been argued. Studies shows that the mass spectroscopy on these samples provided the information about hydrogen desorption possibility at lower temperatures below 100°C , but also other studies have suggested that it is also possible by the desorption of impurities from the pores of γ - $\text{Mg}(\text{BH}_4)_2$.

5. Conclusion and future perspectives

γ - $\text{Mg}(\text{BH}_4)_2$ was heated from temperatures between 240 – 400°C in Ar flow of 200 ml/min with 5 K/min of heating rate with several hours of isothermal reaction time in various temperatures. The glove box was used to handle the air-sensitive γ - $\text{Mg}(\text{BH}_4)_2$ all the times of sample preparations. A combined TGA-DSC instrument was used to heat the sample and to study the reaction kinetics and weight loss during the decomposition. The partially decomposed sample was then studied by using PXD techniques to check whether any crystalline compound is present. The sample prepared in the same measurement conditions were further studied by XAS technique under in synchrotron light source. With TEY XAS measurement at B K-edge, the local structure of boron species was studied. TGA-DSC collectively

provided the information with a maximum of 11.3% of weight loss at 400°C in a maximum of 5- endothermic steps out of those, prepared below this temperature. The reaction at 400°C desorbed 3.1H₂ molecules per reaction leaving MgB₂H_{1.8} as a final intermediate product. But the weight loss has been observed since the beginning of heating, below 100°C. PXD confirmed the complete desorption of H₂ leaving only the amorphous species above 260°C and up to 280°C under these measurement conditions. Presence of only crystalline MgH₂ at 300°C and formation of Mg above 320°C along with the amorphous B-H. XANES on B K-edge spectra collected on total electron yield mode for various references and the samples provided information about the co-ordination and the local environment around B in each compound. From the qualitative comparison of the B K-edge spectra of samples with the references, it was possible to see the presence of amorphous boron in the samples decomposed at 340°C and 400°C. The tetrahedral coordination of B remains in the reaction product from 240- 300 °C but for the sample decomposed at 320°C no peak for tetrahedral boron at around 192 eV is seen suggesting the other stage of reaction with the absence of BH₄⁻ ion. But the broader peak around 192 was observed in the samples decomposed at 340°C and 400°C which could be the combined effect of tetrahedral B (possibly BH₄⁻ ion) with other unknown boron species that could possibly be MgB₁₂H₁₂ as mentioned in [42, 50, 52]

The combined experimental approach indicated the following decomposition mechanism:



The experimental analysis from the combined scientific techniques provided valuable information on the partial decomposition reaction of $\gamma\text{-Mg}(\text{BH}_4)_2$, which certainly has contributed in characterizing the intermediate products from partial decomposition reaction of $\gamma\text{-Mg}(\text{BH}_4)_2$. All the objectives of this thesis have been successfully achieved as planned and the valuable information have been extracted by analyzing the partially decomposed $\gamma\text{-Mg}(\text{BH}_4)_2$. However, the characterization of the intermediate reaction products has been partially accomplished through this work.

For the further analysis, the samples might be investigated by TFY of XAS, Raman, and X-ray photoelectron spectroscopy (XPS). Spectra for B K-edge XANES for Mg (data is already collected in RGBL together with B) can also be analyzed to find out the local environment around Mg-atom. Data analysis of the sample prepared under the same condition and collective results from these additional approaches along with TGA-DSC, TEY of XAS, PXD might provide more insight into this study. Carrying out the experiment by understanding the details of the decomposition reaction and using the proper additives or changing the heating methods or the heating temperature is also possible. The rise of new but easy instrumentation for the XAS experiment for the highly air-sensitive sample would allow the fast, correct, and easy XAS data acquisition.

6. References

- [1] J. Andersson and S. Grönkvist, "Large-scale storage of hydrogen," *International Journal of Hydrogen Energy*, vol. 44, no. 23, pp. 11901-11919, 2019/05/03 2019.
- [2] E. Rivard, M. Trudeau, and K. Zaghbi, "Hydrogen Storage for Mobility: A Review," *Materials*, vol. 12, p. 1973, 06/19 2019.
- [3] V. Yartys and M. Lototsky, "An Overview of Hydrogen Storage Methods," vol. 172, 2003, pp. 75-104.
- [4] O. Zavorotynska, S. Deledda, and B. C. Hauback, "Kinetics studies of the reversible partial decomposition reaction in $\text{Mg}(\text{BH}_4)_2$," *International Journal of Hydrogen Energy*, vol. 41, no. 23, pp. 9885-9892, 2016/06/22/ 2016.
- [5] I. Saldan, "Decomposition and formation of magnesium borohydride," *International Journal of Hydrogen Energy*, vol. 41, no. 26, pp. 11201-11224, Jul 2016.
- [6] M. M. Rana Mohtadi, Timothy S. Arthur, and Son-Jong Hwang, "Magnesium Borohydride: From Hydrogen Storage to Magnesium Batteries."
- [7] O. Zavorotynska, A. El-Kharbachi, S. Deledda, and B. C. Hauback, "Recent progress in magnesium borohydride $\text{Mg}(\text{BH}_4)_2$: Fundamentals and applications for energy storage," *International Journal of Hydrogen Energy*, vol. 41, no. 32, pp. 14387-14403, 2016/08/24/ 2016.
- [8] D. G. L. Soloveichik, "Metal Borohydrides as Hydrogen Storage Materials," Technical Documents p. 6, 2007.
- [9] L. Silvi, "Hydrogen dynamics in complex borohydrides," P.hd, Department of physics, Technical University of Munich, Germany, 2017.
- [10] Y. F. Radovan Cerny, Hans Hagemann, and Klaus Yvon, "Magnesium Borohydride: Synthesis and Crystal Structure," *A journal of German Chemical Society*, Article vol. 46, no. 30, 2007.
- [11] K. Chłopek, C. Frommen, A. Léon, O. Zabara, and M. Fichtner, "Synthesis and Properties of Magnesium Tetrahydroborate, $\text{Mg}(\text{BH}_4)_2$," *Journal of Materials Chemistry - J MATER CHEM*, vol. 17, 01/01 2007.
- [12] R. Mohtadi and S.-i. Orimo, "The renaissance of hydrides as energy materials," *Nature Reviews Materials*, vol. 2, no. 3, p. 16091, 2016/12/13 2016.
- [13] V. N. Konoplev and V. M. Bakulina, "Some properties of magnesium borohydride," *Bulletin of the Academy of Sciences of the USSR, Division of chemical science*, vol. 20, no. 1, pp. 136-138, 1971/01/01 1971.
- [14] K. VN, "Synthesis of magnesium tetrahydroborate," *Inorganic Chemistry* 1980.
- [15] I. Saldan, "Decomposition and formation of magnesium borohydride," *International Journal of Hydrogen Energy*, vol. 41, 05/01 2016.
- [16] R. J. Newhouse, V. Stavila, S.-J. Hwang, L. E. Klebanoff, and J. Z. Zhang, "Reversibility and Improved Hydrogen Release of Magnesium Borohydride," *The Journal of Physical Chemistry C*, vol. 114, no. 11, pp. 5224-5232, 2010/03/25 2010.
- [17] S. Guo, H. Chan, D. Reed, and D. Book, "Investigation of dehydrogenation processes in disordered $\gamma\text{-Mg}(\text{BH}_4)_2$," *Journal of Alloys and Compounds*, vol. 580, pp. S296-S300, 12/01 2013.
- [18] B. David *et al.*, "The structure, thermal properties and phase transformations of the cubic polymorph of magnesium tetrahydroborate," *Physical chemistry chemical physics : PCCP*, vol. 14, pp. 11800-7, 07/25 2012.
- [19] M. Paskevicius *et al.*, "In-Situ X-ray Diffraction Study of $\gamma\text{-Mg}(\text{BH}_4)_2$ Decomposition," *The Journal of Physical Chemistry C*, vol. 116, no. 29, pp. 15231-15240, 2012/07/26 2012.
- [20] J. G. Vitillo, S. Bordiga, and M. Baricco, "Spectroscopic and Structural Characterization of Thermal Decomposition of $\gamma\text{-Mg}(\text{BH}_4)_2$: Dynamic Vacuum versus H_2 Atmosphere," *The Journal of Physical Chemistry C*, vol. 119, no. 45, pp. 25340-25351, 2015/11/12 2015.

- [21] C. Pistidda *et al.*, "Synthesis of amorphous Mg(BH₄)₂ from MgB₂ and H₂ at room temperature," *Journal of Alloys and Compounds*, vol. 508, no. 1, pp. 212-215, 2010/10/15/ 2010.
- [22] D. Louër, "Powder X-Ray Diffraction, Applications," in *Encyclopedia of Spectroscopy and Spectrometry*, J. C. Lindon, Ed. Oxford: Elsevier, 1999, pp. 1865-1875.
- [23] D. Banerjee, "Experimental Techniques in Thermal Analysis Thermogravimetry (TG) and Differential Scanning Calorimetry (DSC)."
- [24] Y. Waseda, E. Mutsubara, and K. Shinoda, *X-Ray Diffraction Crystallography*. Berlin, Germany: Springer, Berlin, Heidelberg. , 2011.
- [25] P. Willmott, *An introduction to Synchrotron Radiation*, First ed. John Wiley & Sons, Ltd, 2011.
- [26] G. A. Cervantes, "The basics of x-rays," *Technical Fundamentals of Radiology and CT: IOP Publishing*, 2016, pp. 1-1-1-5. [Online]. Available: <http://dx.doi.org/10.1088/978-0-7503-1212-7ch1>.
- [27] I. T. I. o. Physics, "Synchrotron Light," p. 4, 2011.
- [28] B. Rupp, *Biomolecular crystallography: principles, practice, and application to structural biology*. Garland Science, 2009, p. 800.
- [29] R. Kakkar, *Atomic and Molecular Spectroscopy: Basic Concepts and Applications*. Cambridge: Cambridge University Press, 2015.
- [30] J. PENNER-HAHN, "X-ray Absorption Spectroscopy."
- [31] M. Newville, "Fundamentals of XAFS," *Consortium for Advanced Radiation Sources, University of Chicago (USA)*[<http://xafs.org>], vol. 78, 01/01 2004.
- [32] C. A. MacDonald, *An Introduction to X-ray Physics, Optics, and Application*. Princeton University Press, June 13, 2017, p. 368.
- [33] M. Busi, "Self-Absorption Correction in Fluorescence EXAFS," Masters, Faculty of Science and Technology, University of Stavanger Stavanger, Norway, 2016.
- [34] J. Als-Nielsen and D. McMorrow, *Elements of Modern X-Ray Physics*, Second ed. Hoboken, UNITED KINGDOM: John Wiley & Sons, Incorporated, 2011.
- [35] J. A.-N. a. D. McMorrow, "A: Scattering and absorption cross-sections," in *Elements of Modern X-ray Physics* New York: Wiley, 2001, pp. 343-348.
- [36] D. T. v. Buuren. (15/03/2017). *X-ray Absorption Spectroscopy*. Available: https://archive.org/details/ucberkeley_webcast_70RHRCe1eRc
- [37] C. LibreTexts. (12/06/2020). *XANES-Theory*. Available: [https://chem.libretexts.org/Bookshelves/Physical_and_Theoretical_Chemistry_Textbook_Maps/Supplemental_Modules_\(Physical_and_Theoretical_Chemistry\)/Spectroscopy/X-ray_Spectroscopy/XANES_-_Theory](https://chem.libretexts.org/Bookshelves/Physical_and_Theoretical_Chemistry_Textbook_Maps/Supplemental_Modules_(Physical_and_Theoretical_Chemistry)/Spectroscopy/X-ray_Spectroscopy/XANES_-_Theory)
- [38] C. LibreTexts. (12/06/2020). *XANES: Application*. Available: [https://chem.libretexts.org/Bookshelves/Physical_and_Theoretical_Chemistry_Textbook_Maps/Supplemental_Modules_\(Physical_and_Theoretical_Chemistry\)/Spectroscopy/X-ray_Spectroscopy/XANES%3A_Application](https://chem.libretexts.org/Bookshelves/Physical_and_Theoretical_Chemistry_Textbook_Maps/Supplemental_Modules_(Physical_and_Theoretical_Chemistry)/Spectroscopy/X-ray_Spectroscopy/XANES%3A_Application)
- [39] L. Zheng, Y.-D. Zhao, K. Tang, C.-Y. Ma, Y. Han, and M.-Q. Cui, "Total electron yield mode for XANES measurements in the energy region of 2.1–6.0 keV," *Chinese Physics C*, vol. 35, no. 2, pp. 199-202, 2011/02 2011.
- [40] J. Stöhr, "Principles, Techniques, and Instrumentation of NEXAFS," in *NEXAFS Spectroscopy*, J. Stöhr, Ed. Berlin, Heidelberg: Springer Berlin Heidelberg, 1992, pp. 114-161.
- [41] "NEXAFS Spectroscopy," vol. vol 25. .
- [42] K. G. Ray *et al.*, "Elucidating the mechanism of MgB₂ initial hydrogenation via a combined experimental–theoretical study," *Physical Chemistry Chemical Physics*, 10.1039/C7CP03709K vol. 19, no. 34, pp. 22646-22658, 2017.
- [43] BRUKER. (07/2020). *X-ray Diffraction and Scattering* Available: <https://www.bruker.com/products/x-ray-diffraction-and-elemental-analysis/x-ray-diffraction.html>
- [44] "TGA-DSC 3+ TGA 2 Reference Manual."

- [45] S. Molodtsov *et al.*, "High-resolution Russian–German beamline at BESSY," *Applied Physics A*, vol. 94, pp. 501-505, 03/01 2009.
- [46] M. Paskevicius *et al.*, "In-Situ X-ray Diffraction Study of gamma-Mg(BH₄)(2) Decomposition," *The Journal of Physical Chemistry C*, vol. 116, p. 15231, 06/26 2012.
- [47] A. a. O. Jain, Shyue Ping and Hautier, Geoffroy and Chen, Wei and Richards, William Davidson and Dacek, Stephen and Cholia, Shreyas and Gunter, Dan and Skinner, David and Ceder, Gerbrand and Persson, Kristin a.,, "The Materials Project: A materials genome approach to accelerating materials innovation," *APL Materials*, vol. 1, p. 011002, 2013.
- [48] M. E. Fleet and X. Liu, "Boron K-edge XANES of boron oxides: tetrahedral B–O distances and near-surface alteration," *Physics and Chemistry of Minerals*, vol. 28, no. 6, pp. 421-427, 2001/07/01 2001.
- [49] Y. Filinchuk, R. C#erny, and H. Hagemann, "Insight into Mg(BH₄)(2) with Synchrotron X-ray Diffraction: Structure Revision, Crystal Chemistry, and Anomalous Thermal Expansion," *Chem. Mater*, vol. 21, 03/01 2009.
- [50] S. Jeong *et al.*, "A Mechanistic Analysis of Phase Evolution and Hydrogen Storage Behavior in Nanocrystalline Mg(BH₄)₂ within Reduced Graphene Oxide," *ACS Nano*, vol. XXXX, 01/10 2020.
- [51] S. Satyapal. (2018). *2017 Annual Progress Report: DOE Hydrogen and Fuel Cells Program*.
- [52] U. Jeffrey J, "IV.C.3 HyMARC (Core): LBNL Effort," in "DOE Hydrogen Fuel Cells Program," Lawrence Berkeley National Laboratory (LBNL), 1 Cyclotron Road, Mail Stop 67R4110 Berkeley, CA 94720 2018.
- [53] D. Li, G. M. Bancroft, and M. E. Fleet, "B K-edge XANES of crystalline and amorphous inorganic materials," *Journal of Electron Spectroscopy and Related Phenomena*, vol. 79, pp. 71-73, 1996/05/01/ 1996.